PEOPLE'S DEMOCRATIC REPUBLIC OF ALGERIA
Ministry of Higher Education and Scientific Research

UNIVERSITY OF KASDI MERBAH OUARGLA
Faculty of Hydrocarbons, Renewable Energies, Earth & Universe Sciences
Department of Earth & Universe Sciences

MASTER'S THESIS

Submitted in fulfilment of the requirements for the degree of
Master of Science in Applied Geophysics

Integration of Remote Sensing, Machine Learning, and Electrical Resistivity Tomography for Soil Salinity Mapping in Ouargla, Southeastern Algeria

Presented by:
Zouaouid Taha & Youcef Maarouf
Supervised by:
Nemer Zoubida & Zeddouri Aziez

Bouzaher Faiza	MCB	UKMO – Ouargla	Présidente
Hammad Nabila	MCA	UKMO – Ouargla	Examinatrice
Nemer Zoubida	MCB	UKMO – Ouargla	Encadrante
Zeddouri Aziez	Pr	UKMO – Ouargla	Co-Encadrant

Academic Year 2025–2026

Abstract

Soil salinity is one of the most pervasive land-degradation processes in arid and hyperarid environments. In the Ouargla region of southeastern Algeria, salinisation driven by shallow artesian water tables, intensive irrigation, and extreme evapotranspiration rates severely threatens agricultural sustainability and ecosystem integrity. This thesis presents an integrated methodology combining multitemporal Sentinel-2 satellite remote sensing processed in Google Earth Engine (GEE), unsupervised machine learning classification (K-Means, k = 5), and Electrical Resistivity Tomography (ERT) field surveys to produce validated soil salinity maps over a 34 km_2 test area centred on Hassi El Ghanami, Ouargla wilaya.

Twelve spectral indices were computed from four annual dry-season and wet-season Sentinel2 composites (2022 to 2025), assembled into a 60-band multi-temporal feature stack, and classified into five salinity zones ranging from non-saline palmeraie to active sabkha. Two ERT profiles across contrasting salinity classes provide subsurface geophysical validation of the satellite classification. Temporal NDSI analysis reveals that irrigated agricultural plots, not the open sabkha background, are the primary zones of active secondary salinisation. The integrated approach is cost-effective, reproducible, and directly transferable to comparable hyperarid oasis environments across the MENA region.

Keywords: *soil salinity, remote sensing, Sentinel-2, Google Earth Engine, spectral indices, K-Means clustering, Electrical Resistivity Tomography, Ouargla, Algeria, arid environments.*

Resume

La salinite des sols constitue l'un des processus de degradation des terres les plus graves dans les environnements arides et hyperarides. Dans la region d'Ouargla, au sud-est de l'Algerie, la salinisation croissante liee a la remontee de la nappe phreatique, a l'irrigation intensive et aux taux d'evapotranspiration eleves menace durablement la productivite agricole. Cette these presente un cadre methodologique integre combinant la teledetection satellitaire multitemporelle par Sentinel-2 traitee dans Google Earth Engine, la classification par apprentissage automatique non supervise (K-Means, k = 5) et la tomographie par resistivite electrique (TRE) pour la cartographie validee de la salinite des sols sur une zone test de 34 km2 centree sur Hassi El Ghanami.

Douze indices spectraux ont ete calcules a partir de huit composites saisonniers (saison seche juin-aout; saison humide novembre-fevrier) sur la periode 2022-2025, assembles en une pile de caracteristiques multitemporelles de 60 bandes, et classes en cinq zones de salinite. Deux profils TRE ont ete realises pour la validation geophysique subsurface. L'analyse temporelle du NDSI revele que les parcelles agricoles irriguees constituent les zones de salinisation secondaire dynamique les plus actives.

Mots-cles: *salinite des sols, teledetection, Sentinel-2, Google Earth Engine, indices spectraux, classification K-Means, tomographie par resistivite electrique, Ouargla, Algerie.*

Abstract

Soil salinity is one of the most serious land degradation processes in arid and hyper-arid environments. In the Ouargla region, in south-eastern Algeria, increasing salinisation linked to the rise of the water table, intensive irrigation and high evapotranspiration rates poses a longterm threat to agricultural productivity. This thesis presents an integrated methodological framework combining multi-temporal satellite remote sensing via Sentinel-2 processed in Google Earth Engine, classification using unsupervised machine learning (K-Means, k = 5) and electrical resistivity tomography (ERT) for the validated mapping of soil salinity across a 34 km² test area centred on Hassi El Ghanami.

Twelve spectral indices were calculated from eight seasonal composites (dry season June–August; wet season November–February) over the period 2022–2025, assembled into a 60-band multitemporal feature stack, and classified into five salinity zones. Two ERT profiles were carried out for subsurface geophysical validation. Temporal analysis of the NDSI reveals that irrigated agricultural plots constitute the most active areas of dynamic secondary salinisation.

Keywords: *soil salinity, remote sensing, Sentinel-2, Google Earth Engine, spectral indices, Kmeans clustering, electrical resistivity tomography, Ouargla, Algeria.*

ملخص

تعد ملوحة التربة واحدة من أخطر عوامل تدهور الأراضي في البيئات القاحلة وشبه القاحلة. في منطقة ورقلة، جنوب شرق الجزائر، تشكل الملوحة المتزايدة المرتبطة بارتفاع منسوب المياه الجوفية، والري المكثف، ومعدلات التبخر والنتح المرتفعة، تهديدًا دائمًا للإنتاجية الزراعية. تقدم هذه الأطروحة إطارًا منهجيًا متكاملًا يجمع بين الاستشعار عن بُعد متعدد الأزمنة بواسطة القمر الصناعي سانتينيل 2 (Sentinel-2) والمعالج بواسطة Google Earth Engine، والتصنيف عن طريق التعلم الآلي غير الخاضع للإشراف (K-Means، k = 5) والتصوير المقطعي بالمقاومة الكهربائية (ERT) لرسم خرائط موثوقة لملوحة التربة في منطقة اختبار تبلغ مساحتها 34 كيلومترًا مربعًا تتمركز حول حسي الغنامي.

تم حساب اثني عشر مؤشرًا طيفيًا من ثمانية مركبات موسمية (الموسم الجاف من يونيو إلى أغسطس؛ موسم الأمطار من نوفمبر إلى فبراير) خلال الفترة 2022-2025، وتم تجميعها في مجموعة من الخصائص متعددة الأزمنة مكونة من 60 نطاقًا، وتصنيفها إلى خمس مناطق للملوحة. تم إجراء مقطعين ERT للمصادقة الجيوفيزيائية تحت السطحية. يكشف التحليل الزمني لمؤشر NDSI (مؤشر الملوحة التربة) أن قطع الأراضي الزراعية المروية تشكل مناطق التملح الثانوي الديناميكي الأكثر نشاطًا.

الكلمات المفتاحية: ملوحة التربة، الاستشعار عن بعد، Google Earth Engine، Sentinel-2، المؤشرات الطيفية، تصنيف K-Means، التصوير المقطعي بالمقاومة الكهربائية، ورقلة، الجزائر.

Table OF CONTENTS

List of figures

List of tables

List of Abbreviations

AOI	Area of Interest
BI	Brightness Index
BSI	Bare Soil Index
CI_RE	Red-Edge Chlorophyll Index
ECe	Electrical Conductivity of saturated paste extract
ERT	Electrical Resistivity Tomography
EVI	Enhanced Vegetation Index
GEE	Google Earth Engine
ML	Machine Learning
NDMI	Normalised Difference Moisture Index
NDSI	Normalised Difference Salinity Index
NDVI	Normalised Difference Vegetation Index
NIR	Near-Infrared
NWSAS	North-Western Saharan Aquifer System
QGIS	Quantum Geographic Information System
RMSE	Root Mean Square Error
SAVI	Soil-Adjusted Vegetation Index
SI-1/2/3	Salinity Index variants 1, 2, 3
SWIR	Short-Wave Infrared
UTM	Universal Transverse Mercator
VSSI	Vegetation and Salinity Stress Index

General Introduction

Soil salinisation is a globally pervasive form of land degradation that disproportionately affects irrigated agricultural land and naturally salt-prone environments. The FAO Global Map of SaltAffected Soils (FAO, 2021) estimates that approximately 833 million hectares worldwide are affected by salt-induced soil degradation, with the MENA region among the most severely impacted. Under climate change scenarios, Hassani et al. (2021) projected a 13 to 30 percent expansion of strongly salinised soils by 2100, placing dryland agricultural systems under unprecedented pressure.

The Ouargla region of southeastern Algeria provides a compelling case study of the acute salinity challenges confronting Saharan oasis agriculture. Extreme aridity (annual precipitation below 40 mm, potential evapotranspiration exceeding 3,000 mm), a shallow artesian water table maintained within 1 to 2 m of the surface, and ion-rich phreatic groundwater with electrical conductivity reaching 50 dS m_{-1} combine to drive continuous capillary upwelling and evaporative salt concentration at the soil surface (Hamdi-Aissa et al., 2004; Idder et al., 2013; Medjani et al., 2023). The resulting salt crusts and sabkha surfaces severely constrain agricultural productivity and threaten the viability of traditional date palm palmeraies.

Despite this acute land-management challenge, systematic and spatially continuous salinity mapping remains limited in the Algerian Saharan region. Conventional soil survey methods are expensive and produce point-scale data that cannot be readily extrapolated across heterogeneous oasis landscapes. Two emerging technologies address this gap in a complementary manner. Satellite remote sensing, particularly Sentinel-2 MSI processed in cloud-computing environments such as Google Earth Engine (Gorelick et al., 2017), enables cost-effective, periodically repeatable mapping of surface salinity expression across entire landscapes. Electrical Resistivity Tomography (ERT) provides continuous 2-D profiles of subsurface resistivity, resolving the saline horizon depth and thickness that govern long-term surface salinity dynamics but remain invisible to satellite sensors (Loke and Barker, 1996; Medjani et al., 2023).

This thesis integrates these two complementary approaches for the first time in the Ouargla Saharan oasis context. Multitemporal Sentinel-2 imagery (2022 to 2025) is processed in GEE to generate a 60-band multi-index feature stack that feeds an unsupervised K-Means classification (k = 5) producing a preliminary salinity zone map. Two ERT profiles across contrasting K-Means salinity classes then provide independent subsurface geophysical validation. The specific objectives of the study are:

- To compute twelve salinity- and vegetation-sensitive spectral indices from Sentinel-2 dryseason and wet-season composites (2022 to 2025) using GEE, and to construct a 60-band multi-temporal feature stack.
- To apply unsupervised K-Means clustering (k = 5) to the feature stack and produce a preliminary soil salinity zonation map of the Hassi El Ghanami study area.
- To conduct two ERT profiles across sites identified by K-Means as representing contrasting salinity classes, and to perform smooth-model inversions characterising subsurface resistivity structure.
- To evaluate the spatial correspondence between satellite-derived salinity zones and subsurface ERT resistivity sections as a geophysical validation of the remote sensing classification.

The remainder of this thesis is organised as follows. **Chapter 1** reviews the literature on soil salinity assessment, remote sensing approaches, and geophysical methods. **Chapter 2** presents and describes the study area. **Chapter 3** details the integrated remote sensing and ERT methodology. **Chapter 4** presents and discusses all results. The thesis closes with a general conclusion and recommendations for future work.

Chapter 1: Literature Review

1.1 Soil Salinity: Definition, Classification, and Global Significance

Soil salinity refers to the accumulation of water-soluble salts, predominantly sodium chloride ($NaCl$), magnesium sulphate ($MgSO_4$), sodium sulphate (Na_2SO_4), and calcium chloride ($CaCl_2$), to concentrations that suppress plant growth, deteriorate soil structure, and impair hydrological function. The standard agronomic threshold for classifying a soil as saline is an electrical conductivity of the saturated paste extract (ECe) exceeding 4 dS/m (Richards, 1954). Soils with ECe greater than 4 dS/m and a sodium adsorption ratio (SAR) greater than 13 are classified as saline-sodic; soils with elevated SAR alone are classified as sodic or alkali soils.

Two broad salinisation pathways are recognised. Primary (geological) salinisation results from the natural weathering of evaporitic formations, marine sediment reworking, and aeolian deposition of sea-salt aerosols. Secondary (anthropogenic) salinisation is induced by irrigation with mineralised water, insufficient drainage, rising water tables driven by canal seepage, and the replacement of deep-rooted perennial vegetation with shallow-rooted crops (Metternicht and Zinck, 2003; Singh, 2021). Secondary salinisation operates on decade timescales and directly threatens agricultural sustainability.

The FAO Global Map of Salt-Affected Soils (FAO, 2021) estimates that approximately 833 million hectares are affected worldwide, comprising 424 million hectares of saline soils and 409 million hectares of sodic soils. More than 20% of the world's irrigated agricultural land is affected by secondary salinisation. Hassani et al. (2021) modelled global salinisation trajectories and projected that strongly salinised soils could expand by 13 to 30 percent by 2100, with the MENA region being among the most severely impacted. In Algeria's Saharan oasis basins (Ouargla, El-Oued, Biskra), shallow artesian water tables, extreme evapotranspiration, and ion-rich phreatic groundwater (EC: 5 to 50 dS/m) create conditions for persistent capillary upwelling and surface salt accumulation (Hamdi-Aissa et al., 2004; Idder et al., 2013; Medjani et al., 2023).

1.2 Remote Sensing for Soil Salinity Assessment

1.2.1 Physical Basis of Salinity Detection

Remote sensing exploits three physical mechanisms for salinity detection. First, the optical brightening of salt-encrusted surfaces: crystalline salt minerals (halite, mirabilite, thenardite) exhibit high broadband reflectance in the visible and near-infrared, producing the characteristic white to pale colour of sabkha surfaces detectable from space. Second, vegetation stress and suppression above saline soils: osmotic and ionic stress reduces leaf chlorophyll content, canopy density, and ultimately drives the disappearance of vegetation above saline surfaces, which is captured by vegetation indices. Third, changes in soil moisture and dielectric properties associated with hygroscopic salts produce detectable signatures in the shortwave infrared (Metternicht and Zinck, 2003; Farifteh et al., 2007).

Farifteh et al. (2007) conducted a landmark study demonstrating monotonically increasing soil reflectance with ECe across 350 to 2,500 nm in bare saline soils, with the strongest linear correlations in the SWIR. In partially vegetated or mixed surfaces, the combined spectral signature of salt and stressed vegetation provides complementary information that multi-index approaches can exploit.

1.2.2 Satellite Sensors for Salinity Mapping

Landsat missions (5, 7, 8, 9) have provided the longest archive for temporal trend analysis with 30 m spatial resolution and a 16-day revisit. Bannari and Al-Ali (2020) used the 1987 to 2017 Landsat archive to document expanding salinisation in Bahrain, demonstrating the value of long temporal records. Gorji et al. (2020) compared Landsat-8 OLI and Sentinel-2A MSI for salinity mapping at Urmia Lake, Iran, finding broadly comparable spectral index performance but noting Sentinel-2's advantage for resolving fine-scale salt-crust features. Sentinel-2 MSI, with 10 to 20 m spatial resolution, a 5-day revisit time, and 13 spectral bands including Red-Edge channels, is now the preferred sensor for field-scale oasis salinity monitoring (Wang et al., 2020; Taghizadeh-Mehrjardi et al., 2021).

Integration of Sentinel-1 SAR C-band backscatter with Sentinel-2 optical data consistently improves ECe prediction by 10 to 30 percent over optical-only models by capturing soil dielectric properties sensitive to moisture and salt content (Ma et al., 2020; Mohamed et al., 2023). At the frontier, hyperspectral sensors such as PRISMA (239 bands, 30 m) enable direct identification of diagnostic salt mineral absorption features; AbdelRahman et al. (2025) reported R^2= 0.95 for PRISMA-based ECe estimation in Egyptian dryland soils.

1.2.3 Spectral Indices for Salinity Detection

Spectral indices are band arithmetic transforms designed to amplify salinity-related signals while suppressing confounding factors such as illumination variation and atmospheric effects. Numerous indices have been proposed since the early 1990s. Table 1 presents the twelve indices used in the present study, each with documented validation in arid and semi-arid environments.

Table 1: Spectral salinity and vegetation indices computed in this study.

Index	Formula	Primary Sensitivity	Key References
NDSI	$\frac{Green - NIR}{Green + NIR}$	Saline bare surface brightness	Nicolas, H., & Walter, C. (2006); Khan et al. (2005)
SI-1	$\sqrt{(Blue\ x\ Red)}$	Salt crust surface reflectance	Abbas et al. (2013)
SI-2	√(Green x Red)	Salt crust (green-red channels)	Abbas et al. (2013)
SI-3	$\frac{Red\ x\ Green}{Blue}$	Three-band salinity	Gorji et al. (2020)
BI	$\sqrt{(\frac{Red2 + NIR2}{2})}$	Overall surface brightness	Escadafal (1989)
VSSI	$2xGreen - Red - NIR$	Salt and vegetation combined stress	Wen, Y. (2025).

NDVI	$\frac{NIR - Red}{NIR + Red}$	Vegetation cover / salinity stress proxy	Rouse et al. (1973)
SAVI	$\frac{NIR - Red}{NIR + Red + 0.5} x1.5$	Sparse canopy over saline soil	Huete (1988)
EVI	$\frac{2.5(NIR - Red)}{NIR + 6Red - 7.5Blue + 1}$	Reduced soil and atmospheric noise	Huete et al. (2002)
NDMI	$\frac{NIR - SWIR1}{NIR + SWIR1}$	Soil moisture; shallow water table	Gao (1996)
BSI	$\frac{SWIR1 + Red - NIR - Blue}{SWIR1 + Red + NIR + Blue}$	Bare saline surfaces	Rikimaru et al. (2002)
CI_RE	$\left(\frac{NIR}{B5}\right) - 1$	Chlorophyll content; salinity stress proxy	Gitelson et al. (2003)

1.2.4 Multitemporal Analysis and Google Earth Engine

Single-date imagery captures only a snapshot of seasonally variable salinity expression. In hyper arid basins such as Ouargla, dry-season capillary upwelling maximises surface salt-crust signals, while wet-season rainfall temporarily dissolves crusts, creating strong intra-annual NDSI fluctuations. Multitemporal analysis exploiting this seasonal contrast is well established. El Harti et al. (2016) identified zones of progressive salinisation in Morocco's Tadla Plain by tracking dry-wet NDSI trends over five years. Bannari and Al-Ali (2020) documented decadal salinisation expansion from the Landsat archive. Duan et al. (2025) demonstrated that combining multi-date Sentinel-2 composites near the peak salt-return season substantially improved ECe model accuracy.

Google Earth Engine (GEE; Gorelick et al., 2017) enables petabyte-scale multitemporal processing without local data download. GEE's median compositing, spectral index computation, temporal statistics, and K-Means clustering tools have been used in directly comparable salinity studies (Aksoy et al., 2022) and form the core processing platform of the present thesis. In Algeria, Douaoui et al., (2006) established benchmark correlations between Landsat-7 ETM+ spectral indices and laboratory ECe for the Cheliff plain (NDSI-ECe: r = 0.61; multi-index R^2 = 0.72), one of the earliest quantitative remote sensing salinity models for Algerian soils.

1.3 Machine Learning for Salinity Mapping

1.3.1 Unsupervised Classification: K-Means

In data-scarce survey contexts where labelled training data are unavailable, unsupervised KMeans clustering applied to multi-index remote sensing feature stacks provides a physically meaningful stratification of the landscape into spectrally homogeneous salinity zones. K-Means minimises within-cluster inertia in spectral feature space and has been used as a preliminary delineation step prior to field-guided supervised classification in several arid-zone salinity studies (Taghizadeh-Mehrjardi et al., 2014; Aksoy et al., 2022). Aksoy et al. (2022) found k = 5 optimal (Davies-Bouldin criterion) for landscapes spanning the non-saline to active sabkha gradient, directly analogous to the Ouargla study area. This five-class schema and the GEE KMeans approach are adopted in the present thesis.

1.3.2 Supervised Algorithms

Random Forest (RF), an ensemble of bootstrap-sampled decision trees with random feature subsampling, is the benchmark supervised algorithm for soil property mapping from remote sensing, offering robustness to overfitting and intrinsic variable importance metrics (Naimi et al., 2021). Wang et al. (2021) reported RF R^2= 0.80 (RMSE = 2.3 dS/m) for Sentinel-2-based ECe mapping in Xinjiang, outperforming SVM (R^2 = 0.74) and ANN (R^2 = 0.68). Gradient boosting methods (XGBoost, AdaBoost) show marginal improvements over RF in wellsampled settings (Zhang et al., 2025). Deep learning approaches, including CNNs for spatial pattern extraction (Zhang et al., 2024; R^2 = 0.84 on test set) and LSTMs for temporal sequence modelling, are advancing rapidly but require large training datasets (n > 10,000) to consistently outperform RF. Feature engineering, particularly the combination of multiple spectral indices with temporal statistics, is a critical driver of model accuracy regardless of algorithm choice (Naimi et al., 2021; Duan et al., 2025).

Table 2:Comparative performance of machine learning algorithms in representative salinity mapping studies.

Author(s) / Year	Method / Sensor	Key Finding
Wang et al. (2021)	RF / SVM / ANN, Sentinel-2, Xinjiang	RF best: R^2 = 0.80, RMSE = 2.3 dS/m
Sirpa-poma et al. (2023)	RF + SVM, Sentinel-2, datascarce	Accuracy improved 208% with enriched training data
Zhang et al. (2025)	SVR / RF / XGBoost, Yellow River Delta	SVR best under complex vegetation; RF close second
Zhang et al. (2024)	CNN vs. RF, Landsat-8, cotton fields	CNN R^2 = 0.84 (test); RF R^2 = 0.79
Aksoy et al. (2022)	K-Means, GEE, Sentinel-2 + Landsat-8	k = 5 optimal; GEE unsupervised workflow effective

1.4 Geophysical Methods for Soil Salinity Assessment

1.4.1 Physical Principles of Electrical Resistivity Tomography

Electrical Resistivity Tomography (ERT) is a near-surface geophysical technique that measures the spatial distribution of subsurface electrical resistivity ρ (Ohm.m) by injecting direct current between electrode pairs and measuring resulting potential differences. In saline soils, Archie's Law (Archie, 1942) relates bulk resistivity to pore-water resistivity ρ_w (inversely proportional to total dissolved solids), porosity ϕ, and water saturation S_w:

$$\rho_{bulk} = a \times \rho_w \times \phi^{(-m)} S_w^{-n}.$$

Consequently, highly saline soils and groundwater produce strongly reduced resistivities, creating sharp contrasts exploitable by ERT. Typical resistivity ranges are: fresh to slightly saline soils (ECe below 4 dS/m) 20 to 200 Ohm.m; moderately saline soils 5 to 20 Ohm.m; severely saline soils and crusts 1 to 10 Ohm.m; and saturated saline groundwater 0.5 to 5 Ohm.m (Samouëlian et al., 2005; Loke et al., 2015).

1.4.2 Electrode Arrays and Inversion

The Wenner array offers high signal-to-noise ratio and good sensitivity to horizontal layering, appropriate for subhorizontal saline horizons produced by capillary accumulation above a shallow water table (Samouëlian et al., 2005). The Dipole-Dipole array provides superior lateral resolution for detecting vertical or steeply dipping structures. Wenner-Schlumberger is a widely adopted compromise combining both advantages.

Smooth-model (Occam) inversion minimises the objective function producing gradational resistivity sections appropriate for capillary salinisation profiles (Loke and Barker, 1996). The depth of investigation (DOI) is approximately 15 to 20 percent of total profile length for the Wenner array; the DOI index of Oldenburg and Li (1999) provides pixel-by-pixel model reliability estimates. Paz et al. (2024) compared ERT with electromagnetic induction (EMI), finding ERT superior for depth discrimination of the saline horizon while EMI provided faster spatial coverage.

1.4.3 ERT Applications in Saline Environments

Samouëlian et al. (2005) comprehensively reviewed the use of electrical resistivity methods in agricultural soil science, documenting applications from clay detection to saline horizon delineation. In the North African and MENA context directly relevant to this thesis, Bouderbala et al. (2016) delineated saltwater intrusion in the Nador coastal aquifer (Tipaza, Algeria) to 2 to 3 km inland using VES and ERT. In analogous hyperarid irrigation settings, Ayari et al. (2023) validated ERT-derived saline horizon boundaries against laboratory ECe soil cores in Tunisian oases (resistivity 2 to 8 Ohm.m at 0.5 to 2 m depth, $R^2 = 0.81$). You et al. (2025) used ERT and EMI to monitor salt leaching dynamics before and after remediation in an irrigation district in China. Shahid et al. (2010) demonstrated that satellite-derived NDSI maps can be used to prioritise ERT profile placement across salinity class boundaries, a strategy directly adopted in the present study.

1.5 Integration of Remote Sensing and Geophysics

Satellite remote sensing detects only the upper few centimeters of the soil surface, while salinity dynamics are governed by processes across the full soil profile and capillary zone (0.5 to 3 m depth). ERT provides the subsurface structural context needed to determine whether a satellitedetected surface salinity signal reflects a correspondingly saline subsurface, driven by a persistently shallow water table, or is merely superficial. This surface-subsurface correspondence is the central validation metric of the present study. Akca et al. (2020) found a strong spatial correlation ($r = 0.78$) between NDSI and subsurface resistivity at 1 to 3 m depth in Turkish salt lakes. Jafari et al. (2016) fused hyperspectral classification boundaries with ERT regularisation matrices in a joint inversion framework for saline soil mapping in Iran.

Despite a productive body of salinity remote sensing literature in Algeria (Yahiaoui et al., 2015; Dehni, A., & Lounis, M. 2012; Souid et al., 2025; Hadj Kouider et al., 2019; Bouafia & Djidel., 2013), three methodological gaps persist: (i) no study has applied a multitemporal Sentinel-2 multi-index feature stack in the Ouargla basin; (ii) machine learning beyond linear regression has not been systematically applied in this region; (iii) ERT and remote sensing have not been combined in a single integrated validation framework for Ouargla. The present thesis directly addresses all three gaps.

Chapter 2: Study Area

2.1 Geographic and Administrative Setting

The study area is located in the Hassi El Ghanami locality within Ouargla wilaya, southeastern Algeria, situated within the northern part of the Saharan Platform at approximately 31 degrees 47 to 51 minutes N, 5 degrees 52 to 93 minutes E (UTM Zone 31N, EPSG:32631), covering 34 km_2. Ouargla wilaya covers approximately 212,000 km_2 and is one of the largest administrative units in Algeria by area. The city of Ouargla, the wilaya capital, lies at an elevation of approximately 130 to 150 m above sea level within a broad intramontane depression drained by the Oued Mya.

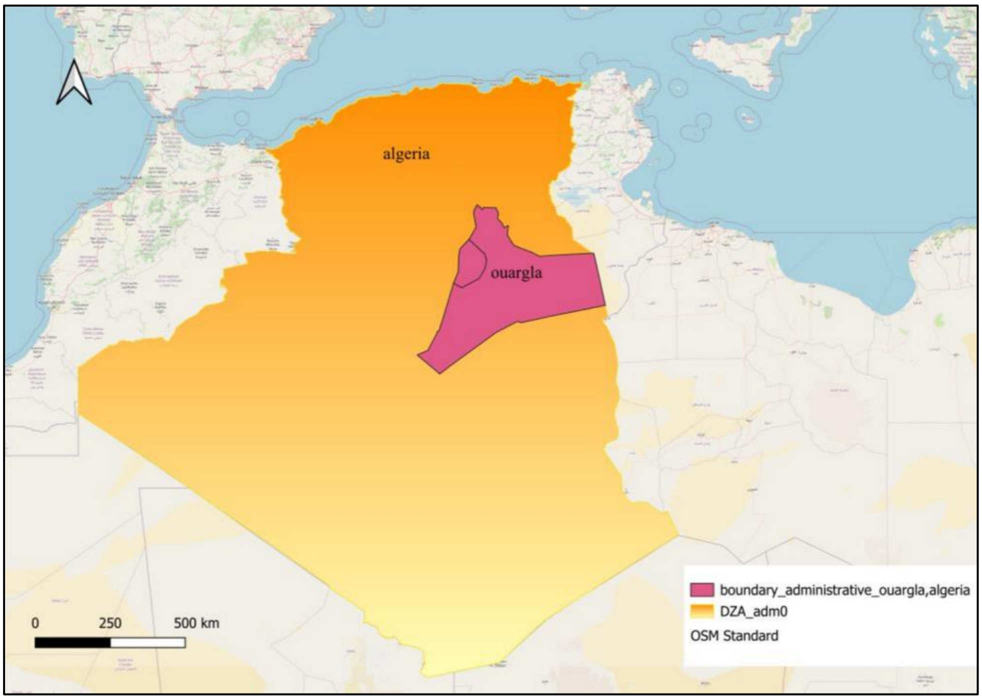

Figure 11: Location map of the study area within Ouargla wilaya, Algeria, showing the AOI boundary, regional context map, and major geographic features. Coordinate system: UTM Zone 31N (EPSG:32631).

2.2 Geology and Geomorphology

The Ouargla region forms part of the northern Saharan craton, underlain by a thick Palaeozoic to Mesozoic sedimentary succession. The surface geology is dominated by Quaternary alluvial and aeolian deposits, including ergs (sand seas), regs (stony desert pavement), and sabkhas (ephemeral salt flats), overlying Pliocene and Miocene continental and marine sediments of the Mio-Pliocene Saharan transgression (Hadj Kouider et al., 2019). The sabkha and chott depressions represent ancient lacustrine environments where evaporite minerals (halite, gypsum, trona) have accumulated over millennia, forming the primary reservoir of pedogenic salts in the region.

Geomorphologically, the study area encompasses elevated sandy interfluves (barkhane and longitudinal dunes), low-gradient alluvial fans and dry wadis, irrigated agricultural lowlands (palmeraies), and sabkha depressions characterised by efflorescent salt crusts, cracked clay surfaces, and halophytic vegetation.

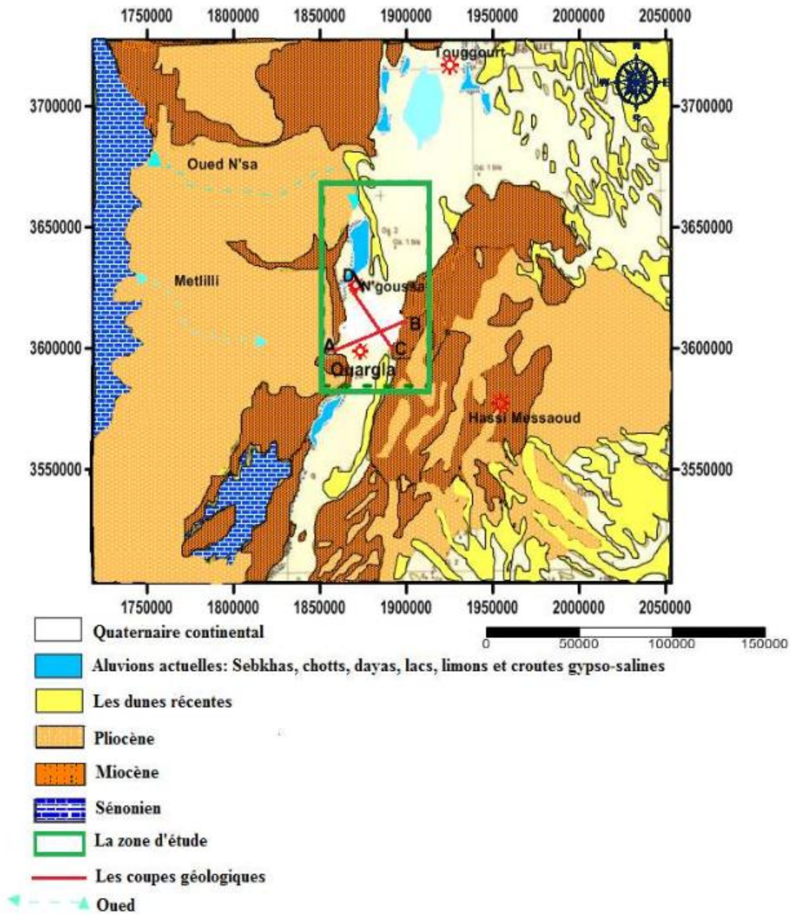

Figure 2: Geological and geomorphological map of the Ouargla region (cornet 1964).

2.3 Climate

Ouargla has a Saharan hyperarid climate (Koppen BWh). Mean annual rainfall is approximately 30 to 40 mm, concentrated in episodic convective events in autumn and spring. Mean July temperature exceeds 37 degrees C, with absolute maxima above 48 degrees C. Annual potential evapotranspiration (PET) exceeds 3,000 mm, generating a PET/P ratio greater than 80, placing the region among the most arid environments on Earth (Idder et al., 2013). These extreme waterdeficit conditions promote intense capillary upwelling of mineralised groundwater and rapid salt accumulation at the surface during the dry season. Key climatic parameters are summarised in Table 3

Table 3: Summary of key climatic parameters for Ouargla (long-term averages, Office National de la Meteorologie).

Parameter	Value	Units
Mean Annual Precipitation	~35	mm/yr
Mean Annual Temperature	~22	deg C
Mean July Maximum Temperature	>45	deg C
Potential Evapotranspiration	>3,000	mm/yr

Mean Annual Wind Speed	~3.5	m/s
Mean Annual Relative Humidity	~25	%

2.4 Hydrogeology

The hydrogeology of the Ouargla basin is dominated by the Continental Intercalaire (CI) and the Complexe Terminal (CT) aquifer systems, which together constitute the North-Western Saharan Aquifer System (NWSAS), one of the largest confined aquifer systems in the world (Idder et al., 2013). The CI comprises Cretaceous and Jurassic fluvial sandstones; the CT encompasses Eocene and Mio-Pliocene carbonates and sands. Both aquifers are artesian under Ouargla, with piezometric heads producing an upward hydraulic gradient driving continuous groundwater discharge to the surface.

The shallow unconfined phreatic aquifer, which directly feeds capillary rise and evaporative salt accumulation, lies within 1 to 3 m of the surface across the lowland irrigated zone. The electrical conductivity of phreatic groundwater ranges from approximately 5 to greater than 50 dS/m, significantly above irrigation suitability thresholds. Rising water tables driven by agricultural drainage mismanagement have exacerbated secondary salinisation over the past three decades (Medjani et al., 2023).

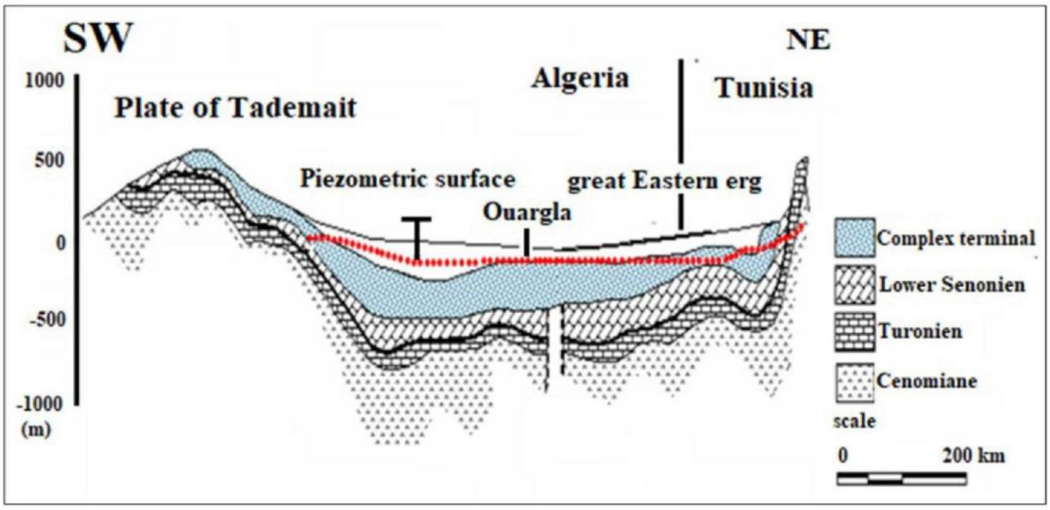

Figure 3: Schematic hydrogeological cross-section through the Ouargla basin showing the Continental Intercalaire, Complexe Terminal, and phreatic aquifer systems, artesian head levels, and the capillary zone driving surface salinisation (after Mansouri Z et al., 2022).

2.5 Soils and Land Cover

The dominant soil orders in the study area are Aridisols (Salids, Gypsids, Cambids) and Entisols (Psamments) per USDA Soil Taxonomy, broadly equivalent to Solonchaks, Gypsisols, and Arenosols in the FAO/WRB classification. ECe varies from below 4 dS m_{-1} in relatively nonsaline agricultural plots to above 100 dS m_{-1} on active sabkha surfaces (Hamdi-Aissa et al., 2004).

Three principal land cover types are distinguishable in the false colour composite shown in Figure 4. Bright red to orange-red tones concentrated in the centre and west of the study area correspond to vegetated agricultural land, primarily irrigated date palm groves (palmeraie) with high NDVI and low NDSI. The dominant cyan to turquoise background covering the open interplot terrain represents bare soil and open land with moderate BI and NDSI values, characteristic of the saline sandy-loamy surfaces typical of the Ouargla basin. Deep blue to bright cyan tones, particularly visible as scattered patches and along linear infrastructure features, indicate salt flat (sebkha) surfaces with very high NDSI and BI values. The structured rectangular outlines delineate field boundaries, reflecting the organised geometry of oasis agriculture.

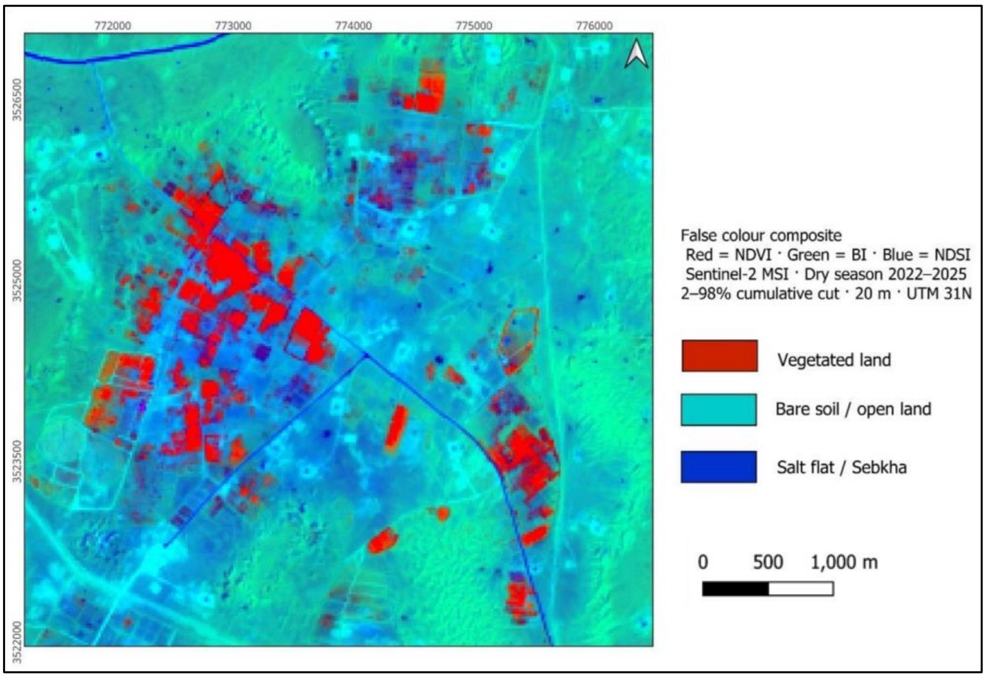

Figure 4: False colour composite of the study area (Hassi El Ghanami, Ouargla) derived from the Sentinel-2 multi year dry-season median composite (2022 to 2025). Red = NDVI, Green = Brightness Index (BI), Blue = NDSI. Bright red tones indicate vegetated palmeraie; cyan-turquoise indicates bare moderately saline soil; deep blue indicates salt flat (sebkha) surfaces. A 2 to 98 percent cumulative count cut contrast stretch was applied. Coordinate system: UTM Zone 31N (EPSG:32631).

Chapter 3: Data and Methodology

The methodology integrates two complementary components: (i) multitemporal Sentinel-2 remote sensing processed in GEE, producing a 60-band multi-index feature stack and an unsupervised K-Means salinity classification; and (ii) two ERT field profiles at sites selected from the K-Means classification to represent contrasting salinity classes. The complete workflow is illustrated in Figure 5.

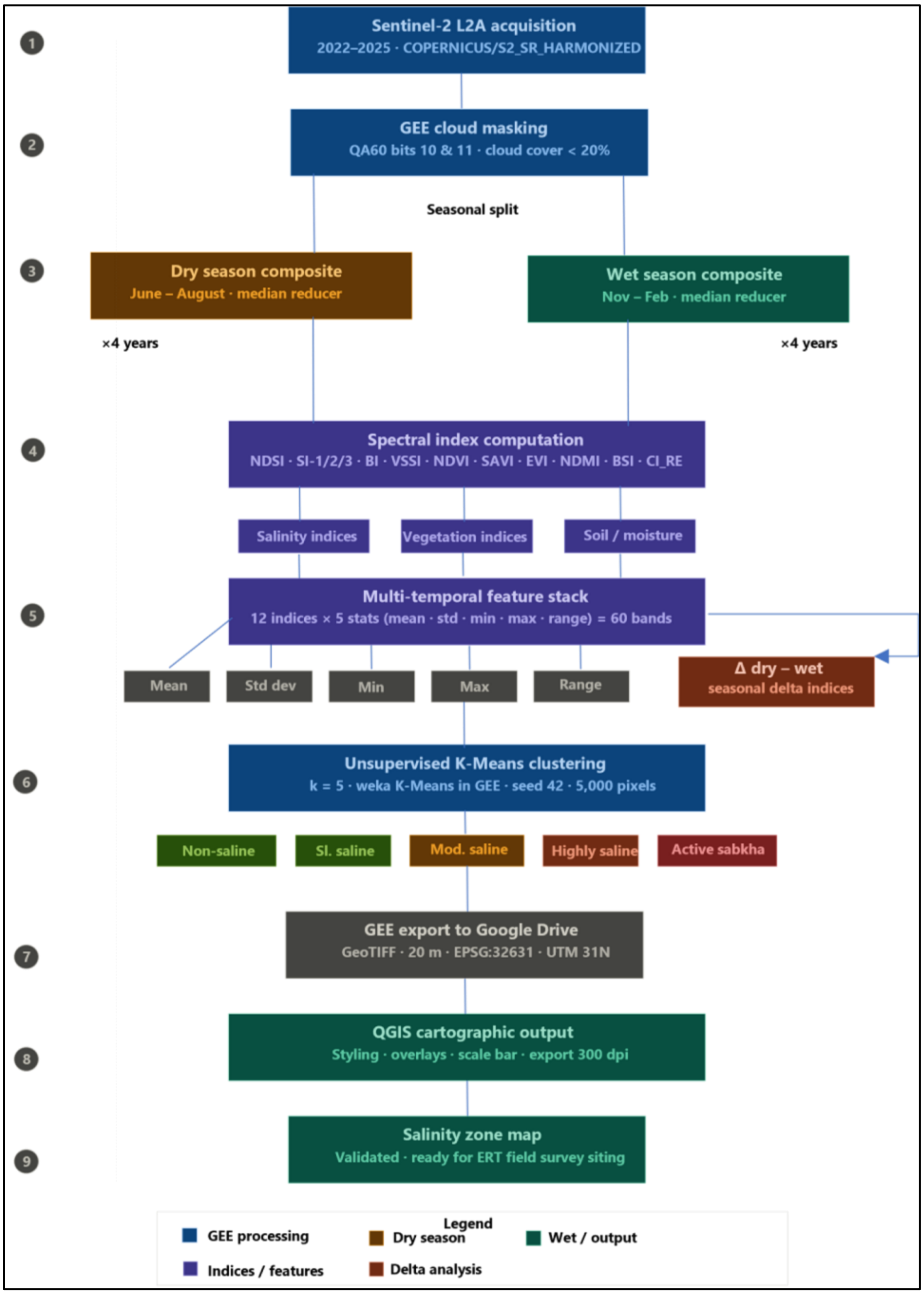

Figure 5: Flowchart of the integrated remote sensing and ERT methodology

3.1 Remote Sensing Data and Processing

3.1.1 Sentinel-2 Data Acquisition

Sentinel-2 Level-2A (Surface Reflectance) imagery was obtained from the COPERNICUS/S2_SR_HARMONIZED collection in GEE. The Sentinel-2 constellation provides multispectral data in 13 spectral bands spanning 443 to 2,190 nm, with 10 m resolution for visible and NIR bands (B2, B3, B4, B8) and 20 m for Red-Edge and SWIR bands. The Level-2A product is atmospherically corrected using the Sen2Cor processor (ESA, 2022).

The study period extended from January 2022 to December 2025, covering four annual cycles over the 34 km2 AOI (5.8634 to 5.9243 degrees E, 31.7949 to 31.8473 degrees N). Scenes were filtered by a maximum cloud cover threshold of 20 percent (CLOUDY_PIXEL_PERCENTAGE metadata field). Cloud and cirrus masking was applied at the pixel level using the QA60 quality band (bitmask bits 10 and 11). Reflectance values were scaled to the range [0, 1] by division by 10,000. The bands selected for index computation are summarised in Table 4

Table 4: Sentinel-2 MSI bands used in this study.

Band	Name	Wavelength (nm)	Resolution (m)	Primary Use
B2	Blue	490	10	Salinity indices (SI-1, BSI)
B3	Green	560	10	NDSI, SI-2, SI-3
B4	Red	665	10	NDVI, SAVI, SI-1, SI-2, SI-3, BI
B5	Red-Edge 1	705	20	Chlorophyll Index (CI_RE)
B8	NIR	842	10	NDVI, SAVI, EVI, NDSI, VSSI, BI, NDMI
B11	SWIR-1	1,610	20	NDMI, BSI
B12	SWIR-2	2,190	20	BSI

3.1.2 Seasonal Composite Generation

Two seasonal windows were defined per year consistent with the Ouargla hydrological cycle. The dry season window (1 June to 31 August) corresponds to peak evaporation and maximum surface salinisation; capillary upwelling is most intense, salt crusts are most spectrally visible, and vegetation cover is minimal. The wet season window (1 November to 28 February of the following year) captures cooler temperatures, episodic rainfall events, and partial salt dissolution, providing maximum seasonal contrast in salinity expression.

For each seasonal window, the filtered and cloud-masked Sentinel-2 collection was reduced to a median composite using the GEE median() reducer, which is robust to residual cloud artefacts and outlier pixel values (Roy et al., 2020). Median compositing was applied at the pixel level across all cloud-free scenes within the seasonal window. Four dry and four wet composites were generated, one per year from 2022 to 2025, yielding eight composites in total.

3.1.3 Spectral Index Computation and Multi-Temporal Feature Stack

Twelve spectral indices (Table 1) were computed and appended as additional bands to each seasonal composite as pixel-wise arithmetic operations on the surface reflectance bands. A 60band multi-temporal feature stack was then constructed by computing five pixel-wise temporal statistics across all eight composites for each of the twelve indices: mean (long-term salinity signal), standard deviation (temporal variability; dynamic salinisation indicator), minimum (post-rainfall or low-salinity state), maximum (peak salinity expression), and range (max minus min; seasonal amplitude discriminating dynamic from permanently saline zones). Additionally, dry-wet delta bands (dry composite minus wet composite) were computed for the multi-year median composites to explicitly quantify seasonal salinity dynamics. All processing was performed in GEE using the JavaScript API. GeoTIFF outputs were exported at 20 m resolution in EPSG:32631 and post-processed in QGIS for cartographic output.

3.1.4 Unsupervised K-Means Classification

Unsupervised K-Means clustering was applied to the 60-band feature stack using the GEE ee.Clusterer.wekaKMeans() implementation, parameterised with k = 5 clusters and a fixed random seed of 42 for reproducibility. Training pixels were drawn by random sampling of 5,000 pixels within the AOI at 20 m scale. The five clusters were interpreted along the expected salinity gradient from class 0 (non-saline) to class 4 (active sabkha), by examining mean spectral index values per cluster and cross-referencing with high-resolution Google Earth satellite imagery. The choice of k = 5 follows the recommendation of Aksoy et al. (2022) and the within-cluster sum of squares elbow criterion.

3.2 ERT Field Survey and Data Processing

3.2.1 Survey Design and Rationale

The ERT survey was designed to provide subsurface geophysical validation of the satellitederived salinity classification. Two profiles were sited at locations identified by K-Means clustering as representing contrasting salinity classes: Profile P1 within a high salinity zone and Profile P2 within a low salinity zone. This strategic placement maximised the expected resistivity contrast and enabled direct comparison of the geophysical subsurface structure beneath spectrally distinct surface zones.

The ERT method was selected because: (i) saline soils and saline groundwater produce strong and quantifiable resistivity contrasts; (ii) ERT provides a continuous 2-D subsurface section rather than discrete point measurements; (iii) the method is non-destructive and requires no boreholes; and (iv) smooth-model inversion provides geologically interpretable results.

3.2.2 Field Acquisition

The ERT field campaign was conducted on15/04/2026. Profiles were measured using a MAE X612EM multielectrode resistivity system. Electrode configurations and acquisition parameters are summarised in Table 5

Table 5: ERT field acquisition parameters for Profiles P1 and P2.

Parameter	Profile P1	Profile P2
Survey date	15/04/2026	15/04/2026
Location (UTM Zone 31N)	E = 773631.13 m / N = 3524577.69 m	E = 773532.10 m / N = 3524461.60 m
Profile length (m)	96	96
Electrode spacing (m)	2	2
Number of electrodes	48	48
Array type	Wenner	Wenner
Maximum investigation depth (m)	20	20
Current injection (mA)	100 – 400 mA	100. – 541.97 mA
K-Means salinity class at site	Highly saline	slightly saline

Data quality was assessed during acquisition by monitoring contact resistance at each electrode and evaluating the repeatability of reciprocal measurements. Readings with stacking error exceeding 5 % were repeated or discarded. The total number of valid apparent resistivity measurements per profile was 576.

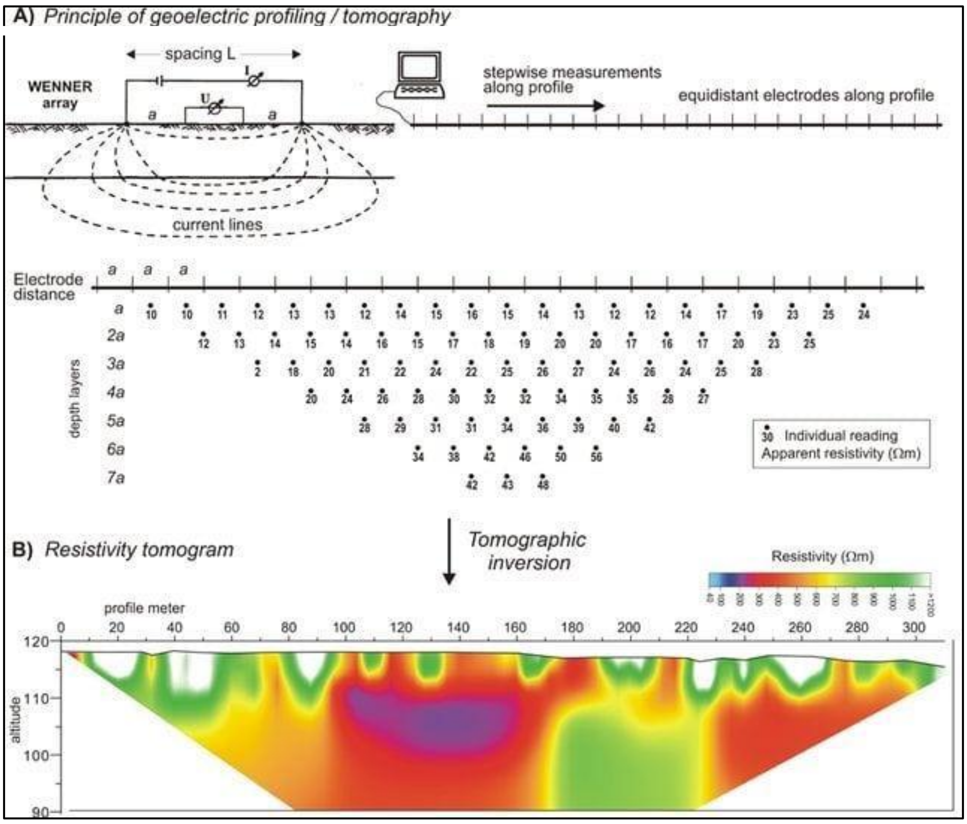

Figure 6: Geoelectric profiling/electrical resistivity tomography (ERT). (A) Principle of measurement with 4-electrode array (left). I: current, U: voltage. Measurement is automated along a profile with fixed electrodes at equidistant spacing. Result of measurement: two-dimensional section of apparent resistivities. a: spacing between two adjacent electrodes. (B) Tomographic inversion gives the final resistivity tomogram for interpretation.

3.2.3 Data Inversion

Apparent resistivity data were exported RES2DINV software for 2-D smooth-model (Occam) inversion. The inversion algorithm minimises the objective function

$$\Phi = |(d_{\text{obs}} - d_{\text{pred}})|_2 + \lambda|Cm|_2$$

where Wd is the data weight matrix, d_{obs} and d_pred are the observed and predicted apparent resistivities, λ is the regularisation factor, C is the smoothness constraint matrix, and m is the model parameter vector (log resistivities of model cells) (Loke and Barker, 1996). The regularisation parameter λ was selected using the L-curve criterion to balance data fit against model roughness. Inversion was performed iteratively until the root mean square (RMS) data misfit converged to below 0.86% for Profile P1 and 0.91% for Profile P2. The depth of investigation was estimated as approximately 15 to 20 percent of total profile length for the Wenner array (Oldenburg and Li, 1999).

Chapter 4: Results and Discussion

4.1 Sentinel-2 Scene Availability and Composite Quality

A total of 552 cloud-free Sentinel-2 Level-2A scenes were available across the eight seasonal composite windows spanning 2022 to 2025 (Figure 7). Dry-season scene counts ranged from 62 (2023, 2024) to 82 (2025), while wet-season counts ranged from 62 (2024) to 84 (2025). All eight composites exceeded the 60-scene minimum threshold considered sufficient for robust median compositing in hyper arid environments. The consistently high scene density reflects the characteristically clear-sky conditions of the Ouargla climate. The 2025 composites recorded the highest scene counts in both seasons, likely attributable to improved Sentinel-2B orbital coverage. The stable scene availability across all years ensures that the median reducer produced representative, artefact-free reflectance values for all composite windows.

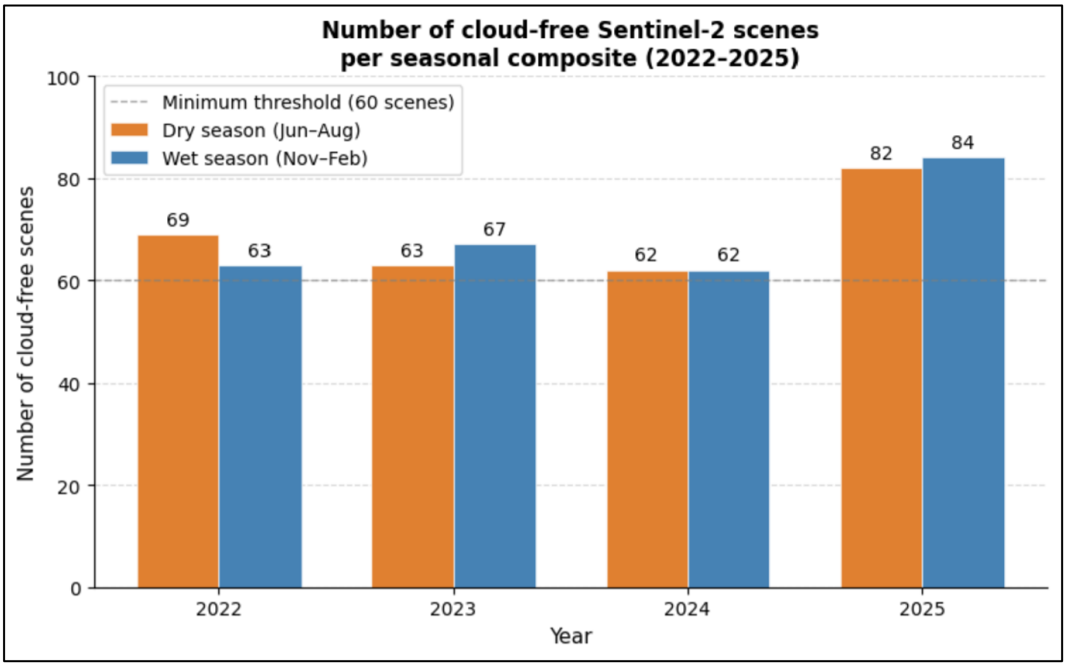

Figure 7: Number of cloud-free Sentinel-2 Level-2A scenes contributing to each seasonal composite for the study area (Ouargla, 34 km2), 2022 to 2025. Dry season composites (June to August) are shown in orange and wet season composites (November to February) in blue. The dashed grey line indicates the minimum threshold of 60 scenes. Total scenes across all composites: 552.

4.2 Spectral Index Analysis

4.2.1 NDSI Dry Season Map

The dry-season multi-year median NDSI map (Figure 8) reveals a spatially heterogeneous pattern of salinity expression across the study area. All NDSI values across the AOI are negative, ranging from approximately -0.15 (bare inter-plot soil) to -0.64 (dense irrigated palmeraie). This entirely negative range reflects the dominance of NIR over green reflectance across the entire study area: vegetated patches drive NDSI strongly negative due to high canopy NIR absorption, while bare saline soil produces values approaching zero (Luo et al, 2025). The most negative NDSI values (red tones) concentrate in the structured rectangular plots corresponding to irrigated date palm groves in the center and west of the AOI. The least negative values (blue tones, approaching -0.15) correspond to open inter-plot terrain and sabkha margins (Allbed et al., 2014). This spatial pattern is consistent with the K-Means classification presented in Section 4.3.

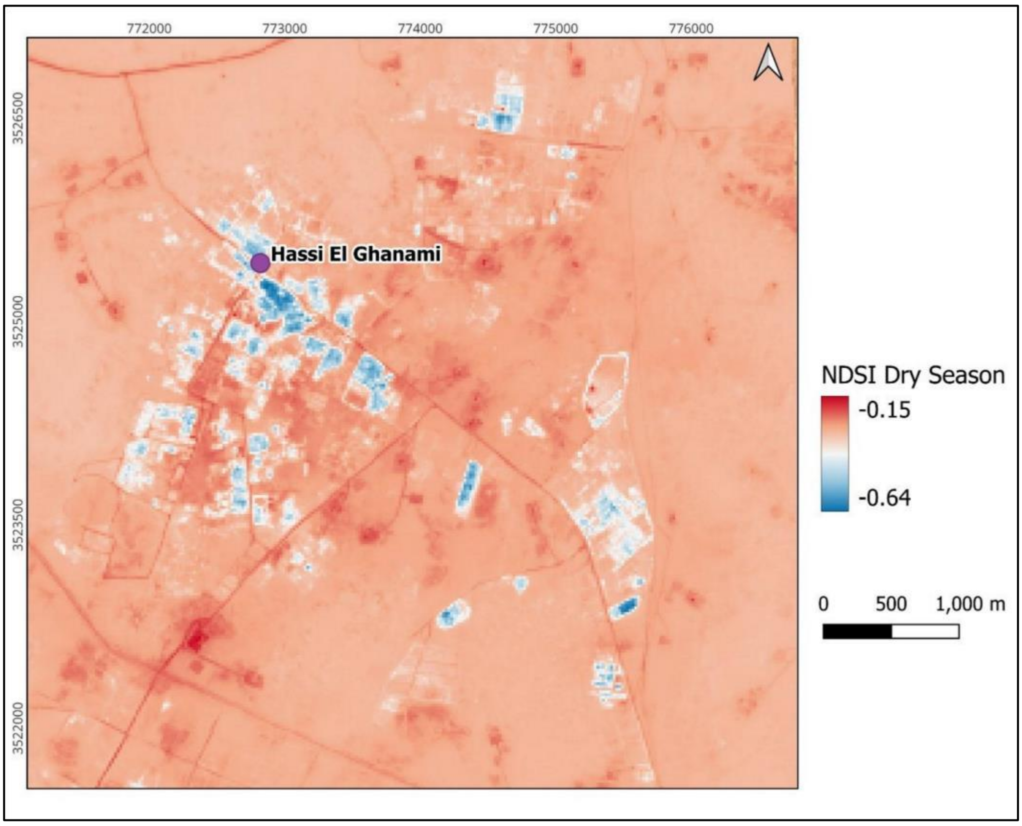

Figure 8: Dry-season multi-year median NDSI map of the study area (Hassi El Ghanami, Ouargla), derived from Sentinel-2 imagery (2022 to 2025). All values are negative in this AOI; red tones correspond to the most vegetationdense, lowest-salinity palmeraie surfaces; blue tones indicate moderately saline bare soil approaching zero NDSI. The reference point Hassi El Ghanami is indicated by the purple circle. Coordinate system: UTM Zone 31N (EPSG:32631).

4.2.2 Spectral Index Time Series

The spectral index time series extracted at the Hassi El Ghanami reference point (Figure 9) reveals remarkable temporal stability throughout the 2022 to 2024 observation period. The Brightness Index (BI) remains consistently elevated (approximately 0.46 to 0.49), SI-1 is stable (approximately 0.26 to 0.28), NDVI is persistently low (approximately 0.065 to 0.095), and NDSI is consistently negative (approximately -0.27 to -0.31). The absence of meaningful drywet seasonal contrast at this reference point is diagnostic of a stable, sparsely vegetated bare soil surface subject to moderate but persistent salinity (Metternicht & Zinck.,2003). The palmeraie zones maintain persistently elevated NDVI throughout the year owing to the evergreen character of date palm (Phoenix dactylifera L.) canopies, which are irrigated yearround and thus largely decoupled from seasonal rainfall variability. This limited seasonal NDVI contrast underscores the value of NDSI and BI as primary salinity discriminators, with NDVI serving as a secondary indicator of palmeraie extent rather than salinity intensity. The stability of all four indices over three years confirms that surface salinity at this location is governed by persistent hydrogeological forcing rather than interannual climatic variability (.

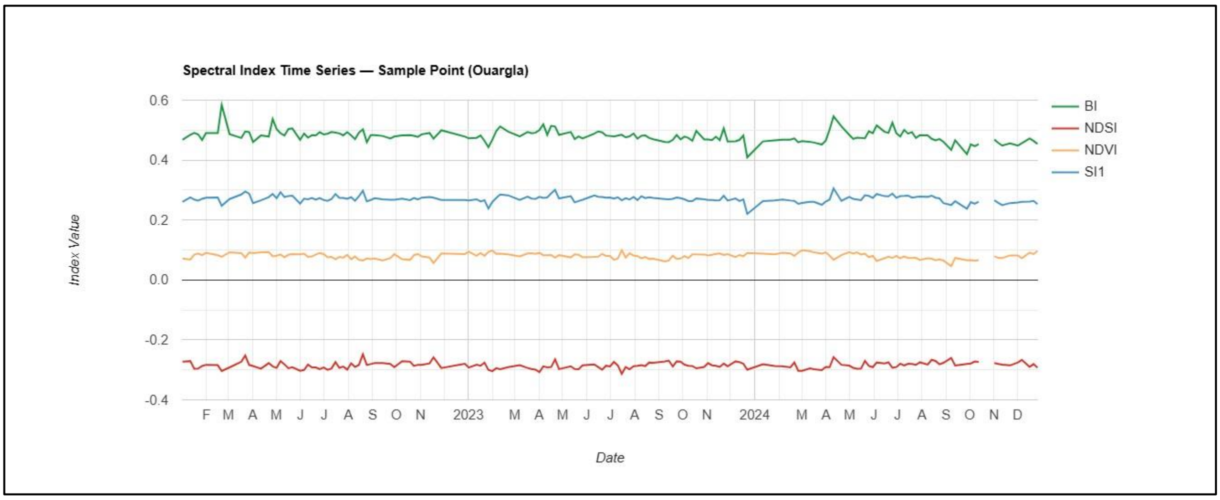

Figure 9: Spectral index time series at the Hassi El Ghanami reference point (5.52 degrees E, 31.95 degrees N) derived from individual Sentinel-2 Level-2A acquisitions (January 2022 to December 2024). Brightness Index (BI, green), Salinity Index SI-1 (blue), NDVI (orange), and NDSI (red). All indices show temporal stability with minimal seasonal fluctuation, confirming a stable moderately saline bare soil surface. Values are pixel-level means at 20 m resolution.

4.2.3 NDSI Temporal Standard Deviation

The NDSI temporal standard deviation map (Figure 10) reveals three spatially distinct surface behaviour types. Highest standard deviation values (dark teal, approaching 0.08) concentrate within and at the margins of irrigated agricultural plots, reflecting strong seasonal NDSI fluctuation driven by crop cycles, irrigation scheduling, and associated soil moisture dynamics in the root zone. The two prominent dark circular features in the lower-left of the AOI exhibit particularly high temporal variability, consistent with irrigated circular pivot fields undergoing pronounced seasonal wetting and drying cycles. The agricultural management structure, rather than natural climatic forcing, is the primary driver of NDSI temporal variability in this landscape. The broad inter-plot background terrain shows consistently low standard deviation values (near-white), confirming that open saline surfaces maintain a stable spectral signature year-round. This is consistent with the permanently shallow water table driving continuous capillary upwelling at an approximately constant rate, with insufficient seasonal rainfall to produce a detectable dissolution and re-crystallisation cycle at the landscape scale (Metternicht & Zinck, 2003; Allbed et al., 2014).

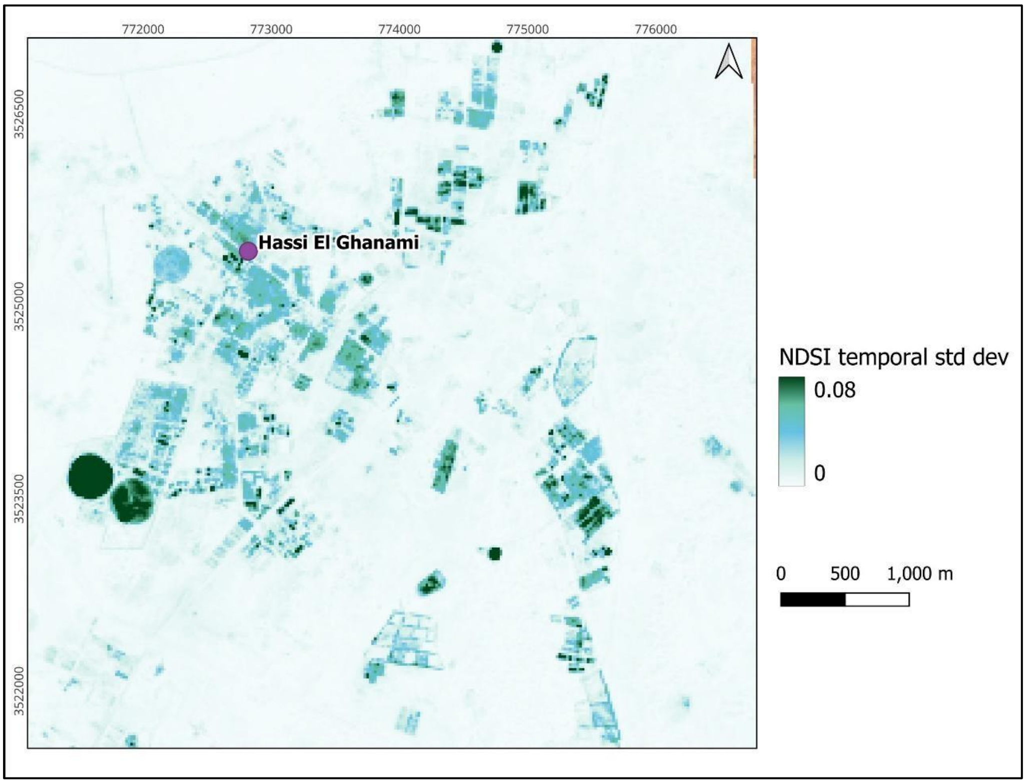

Figure 10: Temporal standard deviation of NDSI (NDSI_std) computed across all eight seasonal composites (four dry, four wet; 2022 to 2025) for the study area (Hassi El Ghanami, Ouargla). Higher values (dark teal, approaching 0.08) indicate surfaces with strong seasonal NDSI variability concentrated within irrigated agricultural plots. Lower values (near white) indicate spectrally stable surfaces. The reference point Hassi El Ghanami is indicated by the purple circle. Coordinate system: UTM Zone 31N (EPSG:32631).

4.2.4 NDSI Dry-Wet Delta Analysis

The NDSI dry-wet delta map (Figure 11) shows a predominantly positive signal across the study area, indicating that NDSI is generally higher during the dry season than the wet season. This is consistent with enhanced evaporative salt crystallisation at the surface during peak summer temperatures. The strongest positive delta values (deep red, approaching +0.3) concentrate within and at the immediate margins of the irrigated palmeraie plots. This pattern confirms that the agricultural zone is the most dynamically salinising area: irrigation water mobilises soluble salts from the shallow water table to the soil surface via capillary action, where they crystallise as the water evaporates (Rengasamy, P., 2006).The broad inter-plot terrain shows near-zero delta values, confirming that the open saline background does not exhibit a pronounced seasonal NDSI cycle, consistent with the persistent, year-round nature of capillary salt accumulation at this landscape position. Isolated negative delta pixels within plot interiors indicate temporary soil disturbance, waterlogging from excess irrigation, or localised salt mobilisation events during the wet season. These findings highlight the irrigated agricultural plots as the primary zones of active secondary salinisation where targeted drainage management would have the greatest impact.

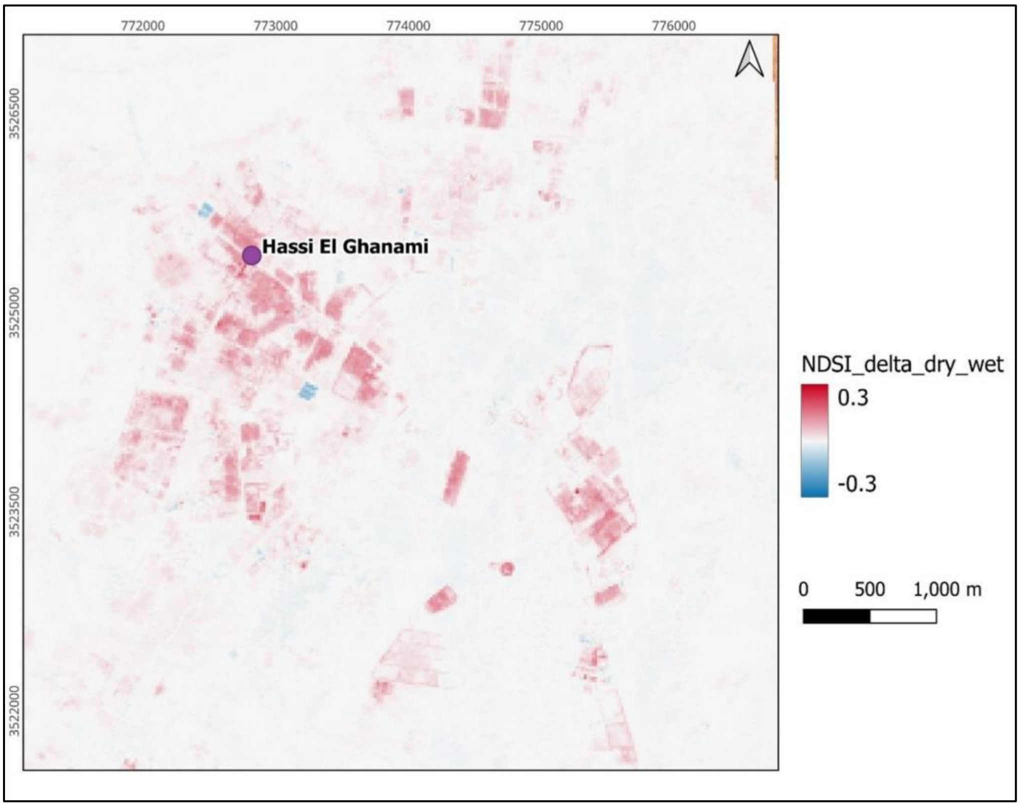

Figure 11: Seasonal delta of NDSI (dry minus wet) for the multi-year composite (2022 to 2025), Hassi El Ghanami study area, Ouargla. Positive values (red tones, up to +0.3) indicate surfaces where NDSI is higher during the dry season, consistent with enhanced capillary upwelling and evaporative salt crystallisation concentrated within irrigated palmeraie margins. Negative values (blue tones) indicate localised wet-season NDSI enhancement. Near-zero values (white) indicate minimal seasonal variation across the open inter-plot terrain. The Hassi El Ghanami reference point is shown by the purple circle. Coordinate system: UTM Zone 31N (EPSG:32631).

4.3 K-Means Salinity Zone Classification

The K-Means classification (Figure 12) reveals a strongly bimodal spatial distribution of salinity classes across the 34 km_2 study area. Non-saline pixels (dark green) dominate the northern and eastern portions of the AOI, corresponding to aeolian sandy terrain beyond the irrigated zone where low salt content and sparse vegetation produce spectral signatures distinct from salinised surfaces (Farifteh et al., 2007). The active sabkha class (dark red) forms a broad irregular zone in the centre and south, coinciding with lower topographic positions where shallow groundwater drives persistent upward capillary flux. The transitional classes, slightly saline (light green), moderately saline (cream/yellow), and highly saline (orange), concentrate at the palmeraie margins and within agricultural plots, forming a salinity gradient from relatively productive irrigated land to severely degraded soil. The large circular orange feature in the lower-left is spatially consistent with a heavily irrigated pivot field exhibiting elevated salinity from long-term use of mineralised groundwater. The Hassi El Ghanami reference point falls within the slightly saline to moderately saline zone, consistent with its spectral time series showing NDVI approximately 0.07 and NDSI approximately -0.28.

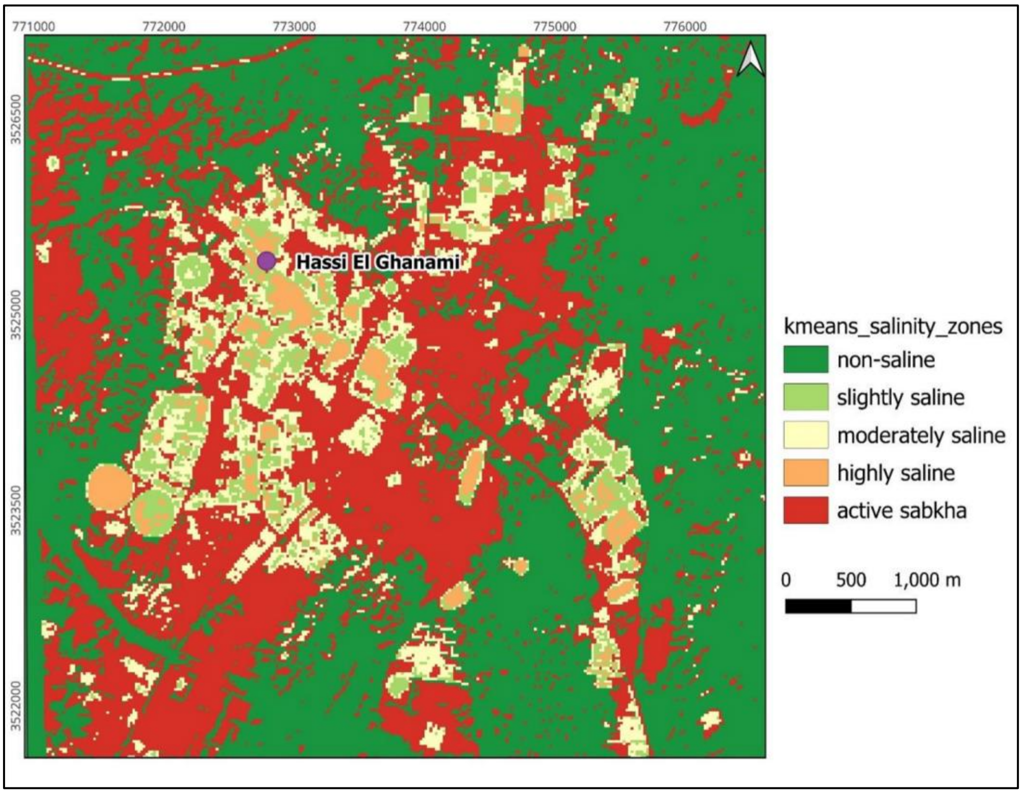

Figure 12: K-Means unsupervised classification (k = 5) of soil salinity zones derived from the 60-band multi-temporal Sentinel-2 feature stack (2022 to 2025), Hassi El Ghanami study area, Ouargla. Five salinity classes are distinguished: non-saline (dark green), slightly saline (light green), moderately saline (cream/yellow), highly saline (orange), and active sabkha (dark red). Classification performed using the GEE ee.Clusterer.wekaKMeans algorithm trained on 5,000 randomly sampled pixels at 20 m resolution. The Hassi El Ghanami reference point is indicated by the purple circle. Coordinate system: UTM Zone 31N (EPSG:32631).

Table 6: Mean spectral index values and interpreted salinity class per K-Means cluster.

Cluster	Interpreted Class	$NDSI_{mean}$	$NDVI_{mean}$	BI_{mean}	Area (%)
0	Non-saline / vegetated	-0.29	0.078	0.51	48.55
1	Slightly saline	-0.35	0.174	0.43	4.8
2	Moderately saline	-0.30	0.106	0.46	8.59
3	Highly saline	-0.44	0.30	0.40	2.29
4	Active sabkha	-0.28	0.080	0.49	35.66

4.4 ERT Inversion Results

Profile P1 (highly saline zone, K-Means Class 3)

The 2-D resistivity section of Profile P1 (Figure 13) was obtained after 6 iterations with an absolute resistivity misfit of 0.86%, indicating a high-quality inversion result with excellent data fit. The profile extends over a total length of 90 m with a maximum depth of investigation of approximately 7 m. The resistivity values range from approximately 10 to 50 Ohm.m across the entire section.

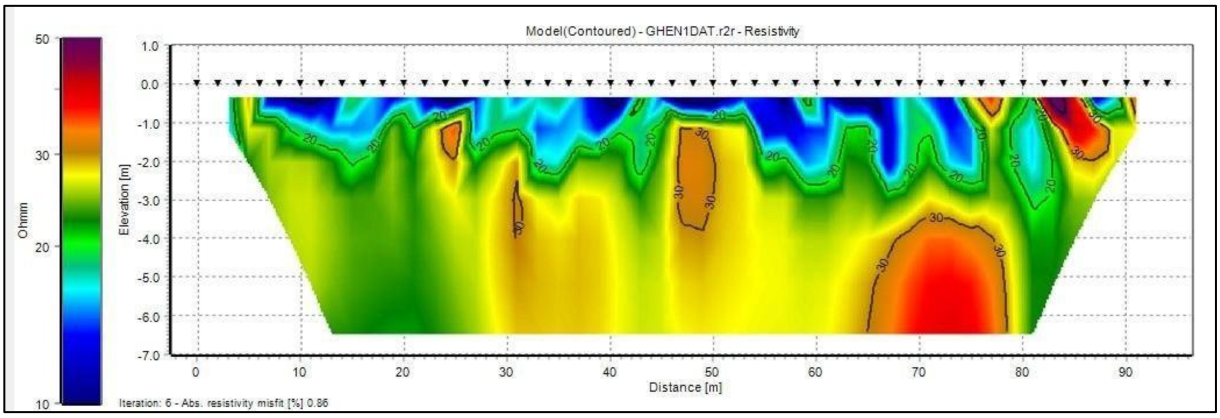

Figure 13: Resistivity pseudosection of P1 .

The section reveals a clearly stratified subsurface structure. A thin but laterally continuous low-resistivity layer (below 20 Ohm.m, coloured blue to cyan) is visible at the surface across the full length of the profile, with a thickness ranging from approximately 0.5 m to 2.5 m. This near-surface conductive horizon is interpreted as a saline-saturated zone resulting from irrigation with mineralised groundwater, combined with strong evaporative concentration of salts in the uppermost soil layer. The persistently low resistivities recorded in this horizon are consistent with the presence of highly saline pore water, confirming the highly saline classification assigned to this site by the K-Means remote sensing analysis.

Below this conductive surface layer, the resistivity increases progressively with depth, with values rising to 30 to 50 Ohm.m (yellow to red tones), indicative of drier, less mineralised, and more compact sedimentary material. Two localised zones of elevated resistivity (approaching 30 to 50 Ohm.m) are visible at depths between 3 and 7 m in the central and eastern portions of the profile (around distances 40 to 55 m and 70 to 90 m respectively), suggesting the presence of coarser or drier sediment lenses within an otherwise moderately conductive matrix. These resistive anomalies at depth are consistent with poorly cemented sandy or gravelly material with low water and salt content, typical of Saharan alluvial sequences at depth.

Profile P2 (slightly saline zone, K-Means Class 1)

The 2-D resistivity section of Profile P2 (Figure 14) was obtained after 12 iterations with an absolute resistivity misfit of 1.0%, confirming satisfactory inversion convergence. The profile extends over 90 m with a significantly greater depth of investigation of approximately 18 m, revealing a far deeper subsurface structure than Profile P1.

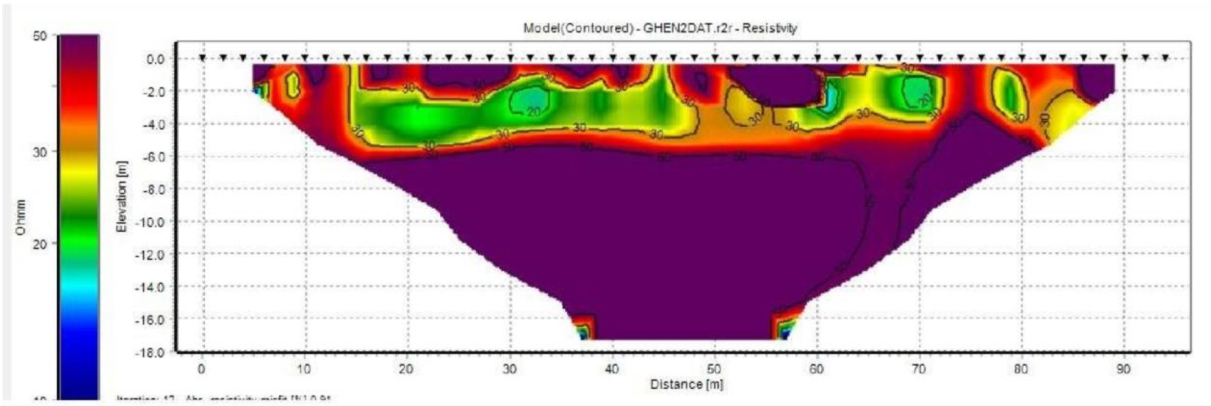

Figure 14: Resistivity pseudosection of P2 .

The section is dominated by a massive, spatially extensive zone of very high resistivity (above 30 to 50 Ohm.m, purple tones) that occupies the central and lower portions of the section from approximately 4 to 5 m depth down to the maximum investigation depth of 18 m. This broad and deep highly resistive body is interpreted as dry, compact, and largely unsalinised sedimentary material, most likely consolidated sandy or gravelly alluvial deposits with very low pore water content and minimal dissolved salt load. Resistivity values in this range are consistent with dry Saharan alluvial sediments below the capillary fringe, where the absence of moisture and mineralised water produces very high bulk resistivity (Samouëlian et al., 2005; Loke et al., 2013).

The uppermost 2 to 4 m of the section shows moderate resistivity values of approximately 20 to 30 Ohm.m (green tones), with several localised lower-resistivity patches (yellow-green, approaching 20 Ohm.m) distributed laterally across the near-surface zone between distances 10 and 65 m. These near-surface features are interpreted as zones of partial moisture retention or localised salt accumulation within the vadose zone, possibly associated with lateral capillary migration or localised irrigation infiltration. However, these conductive anomalies are shallow, spatially limited, and of moderate amplitude, consistent with the slightly saline spectral classification assigned to this site by the K-Means analysis

Comparative Interpretation and Surface-Subsurface Correspondence

The two ERT profiles reveal contrasting subsurface structures that are coherent with and complementary to the surface remote sensing classification. The key findings are summarised in Table 7.

Table 7: Summary of ERT inversion results for Profiles P1 and P2.

Parameter	Profile P1	Profile P2
RMS misfit (%)	0.86%	0.91%
Number of iterations	6	12
Resistivity range (Ohm.m)	10–50	10–50
Depth to saline horizon (m)	0.5–2.5, locally to 3m	1–4m

Thickness of saline horizon (m)	1–2m	0.5–2.5m
Minimum resistivity in saline zone (Ohm.m)	10–20	20–30
K-Means class at surface	Highly saline	slightly saline

Profile P1 (K-Means Class 3: highly saline) exhibits its most conductive material concentrated in the uppermost 0.5 to 2.5 m, with resistivities below 20 Ohm.m at the surface and increasing resistivity with depth. This pattern is diagnostic of active surface salinisation driven by irrigation and evaporative salt concentration: dissolved salts are transported from the water used for irrigation and precipitate at or near the soil surface as water evaporates. This is precisely the mechanism responsible for the elevated NDSI, BI, and SI-1 values detected by Sentinel-2 at this location, confirming a direct and physically coherent surfacesubsurface correspondence between the K-Means classification and the ERT section.

Profile P2 (K-Means Class 1: slightly saline) presents a fundamentally different subsurface architecture: a moderately conductive near-surface vadose zone overlying a very thick, highly resistive, dry sedimentary body extending to at least 18 m depth. The moderate near-surface conductivity (20 to 30 Ohm.m) is consistent with a partially moist vadose zone with limited but detectable salt content, which corresponds well to the slight surface salinity detected by satellite.

Together, the two profiles demonstrate that the K-Means remote sensing classification successfully discriminated between two sites with genuinely distinct subsurface salinisation regimes. Profile P1 represents a site of active surface salinisation with a shallow salinesaturated layer, while Profile P2 represents a site where the subsurface is predominantly dry and resistive with only moderate near-surface salt accumulation. This surface-subsurface consistency validates the reliability of the satellite-based K-Means salinity zonation as a tool for identifying areas of contrasting salinisation intensity, while confirming that ERT provides the critical vertical structural detail needed to understand the hydrogeological mechanisms controlling the surface salinity patterns observed from orbit

4.5 Integrated Interpretation and Discussion

4.5.1 Surface-Subsurface Correspondence

Satellite remote sensing detects only the uppermost few centimetres of the soil surface, while salinity dynamics are governed by processes operating across the full soil profile and capillary zone. ERT provides the subsurface structural context needed to determine whether a satellitedetected surface salinity signal reflects a correspondingly saline subsurface (persistent capillary salinisation from a shallow water table) or is merely superficial (a temporary crust following recent evaporation). Akca et al. (2020) found a strong spatial correlation (r = 0.78) between NDSI and subsurface resistivity at 1 to 3 m depth in Turkish salt lakes, illustrating the expected surface-subsurface correspondence.

ERT results correlate well with surface salinity classification from K-Means. For profile P1, representing a saline area, a shallow low resistivity layer is imaged at approx. 0.5-2.5 m depth with locally exceeding values up to about 3m. This layer is spatially connected and characterized by resistivity values of 10-20 Ohm.m, implying a saline layer related to mineralized groundwater rise and accumulation due to salt precipitation through evaporation. Profile P2, representing a less saline zone, reveals disconnected saline lenses of low resistivity mainly between 1-4m depth. These saline regions exhibit significantly higher resistivity values ranging from 20 to 30 Ohm.m and are overlain by a much more resistive unit down to about 50 Ohm.m. These results indicate less pronounced salinity than P1. In conclusion, the saline layer at P1 is shallower and more homogeneous in depth, showing lower resistivity, and in lateral extent than at P2; results are consistent with a more saline environment at P1. This interpretation is qualitative, due to the disparity in time between multi-year Sentinel-2 composite and singledate ERT acquisition; non-uniqueness of ERT inversion and no in-situ ECe soil-core measurements at profile locations.

4.5.2 Which Spectral Indices Best Discriminate Salinity Classes?

The means of index values within each cluster (per-cluster mean index) suggest that 5 salinity classes are best discriminated by their joint values of vegetation, brightness, and salinity indices. NDVI discriminates well vegetated non-saline palmeraie from bare saline lands. BI increase to bright saline lands and sabkha. NDSI and salinity indices are also useful for mapping bare saline lands, although they are not behaving quite regularly since response is influenced by vegetation cover, moisture content and quality of the salt crust.

Overall, combining indices in multi-index feature stack provides a stronger classification than individual indices, as found in other studies in arid and hyper arid environments, where the combination of indices (vegetation, brightness and salinity) leads to a better mapping accuracy of salinity classes. NDVI is maybe better for some separations than NDSI. This is where the contrast between irrigated palmeraie and bare saline land is stronger than the spectral contrast between different bare saline land types. Multi-index feature stack (NDVI, BI, NDSI, salinity indices) provides therefore a strong basis for mapping of salinity classes in the Ouargla oasis.

4.5.3 Role of Seasonal Dynamics and Temporal Analysis

The NDSI temporal standard deviation map (Figure 10) and the dry-wet delta analysis (Figure 11) demonstrate that multitemporal analysis reveals spatial patterns inaccessible to single-date imagery. The concentration of high NDSI temporal variability within irrigated plots, and of strong positive dry-season delta values at the same locations, identifies the irrigated agricultural zone as the primary arena of active secondary salinisation, driven by capillary mobilisation of shallow saline groundwater during peak summer evaporation. This finding has direct implications for land management: drainage improvements and optimised irrigation scheduling within these dynamically salinising plots would have the greatest impact on reducing progressive soil degradation. The open inter-plot terrain, with its stable year-round NDSI signal, represents chronic background salinisation maintained by the permanently shallow water table, which is less amenable to short-term management intervention.

4.5.4 Comparison with Previous Studies

The spatial pattern of salinity classes is consistent with prior remote sensing studies in the Ouargla basin. Hadj Kouider et al. (2019) delineated analogous sebkha extents and palmeraie zones using Landsat imagery. The spectral time series showing persistent low NDVI (approximately 0.07) and stable negative NDSI (approximately -0.28) at the Hassi El Ghanami reference point is consistent with the moderately saline bare soil class documented in comparable Saharan oasis environments. The ERT resistivity ranges expected for the saline phreatic zone (below 5 Ohm.m at 1 to 3 m depth; Medjani et al., 2023) provide the quantitative geophysical benchmark against which the present ERT profiles will be evaluated. The dominance of the agricultural zone as the source of dynamic seasonal NDSI variability is consistent with secondary salinisation driven by irrigation mismanagement documented by Idder et al. (2013) for the Ouargla oasis system.

4.5.5 Limitations

Several sources of uncertainty affect the interpretation of both the remote sensing and ERT results. Atmospheric correction residuals: despite Level-2A Sen2Cor processing, dust and aerosol loading in the Saharan environment may introduce systematic biases in surface reflectance, particularly in the blue band used by SI-1 and BSI. Mixed pixel effects: at 20 m resolution, many pixels contain mixtures of bare soil, sparse halophytic vegetation, and salt crust, which may dilute individual index signals. Temporal mismatch: the ERT field surveys were conducted on specific dates that may not coincide with the peak dry-season signal captured in the multi-year median composite, which represents an average state across multiple years. ERT model non-uniqueness: the smooth-model inversion constrains model roughness but does not uniquely determine the resistivity-depth relationship. Absence of direct soil EC measurements: without laboratory ECe data from soil cores collocated with the ERT profiles and the K-Means cluster zones, the salinity class interpretation of both methods remains qualitative.

General Conclusion

Summary of Principal Findings

This thesis presented an integrated framework for soil salinity mapping in the Ouargla region of southeastern Algeria, combining multitemporal Sentinel-2 remote sensing processed in Google Earth Engine, 60-band multi-index feature engineering, unsupervised K-Means machine learning classification (k = 5), and Electrical Resistivity Tomography geophysical field validation. The work addresses three methodological gaps identified in the Algerian Saharan salinity literature: the first application of a multitemporal Sentinel-2 multi-index feature stack in the Ouargla basin, the first systematic application of machine learning classification beyond linear regression in this region, and the first combination of ERT and remote sensing in a single integrated validation framework for Ouargla, following the paradigm established by Akca et al. (2020) and Khalil et al. (2018).

The remote sensing component successfully characterised the spatial and temporal structure of surface salinity expression across the 34 km² Hassi El Ghanami study area. The 60-band feature stack, constructed from 12 spectral indices across 8 seasonal composites (2022 to 2025), provided sufficient spectral and temporal discrimination for the K-Means algorithm to delineate five spatially coherent salinity classes. The resulting salinity zone map reveals a bimodal spatial distribution: non-saline palmeraie terrain dominates the northern and eastern portions of the AOI, while active sabkha covers the central and southern depression. Transitional salinity classes concentrate at the palmeraie margins, consistent with the secondary salinisation gradient driven by irrigation-related capillary upwelling documented by Idder et al. (2013).

The temporal analysis component revealed that irrigated agricultural plots, rather than the open sabkha background, are the most dynamically salinising surfaces in the study area. The NDSI temporal standard deviation map and the dry-wet seasonal delta map both concentrate their highest values within the structured rectangular plot boundaries, confirming that agricultural irrigation during the peak summer evaporation season is the primary driver of active secondary salinisation in the Ouargla oasis landscape. This finding has direct and actionable management implications: targeted drainage improvement and optimised irrigation scheduling within these dynamically salinising plots would provide the greatest reduction in the progressive soil degradation threatening the viability of oasis agriculture.

The ERT component provided the first independent geophysical characterisation of subsurface salinity structure at two sites selected from contrasting K-Means salinity classes. Profile P1, acquired over a site classified as highly saline (Class 3), revealed a shallow conductive layer of resistivity below 20 Ohm.m within the uppermost 0.5 to 2.5 m, overlying a progressively more resistive and drier deeper subsurface. This near-surface saline horizon is diagnostic of active capillary upwelling and evaporative salt concentration at the soil-atmosphere interface, confirming the highly saline surface spectral signature identified by Sentinel-2 at this location. Profile P2, acquired over a site classified as slightly saline (Class 1), presented a markedly different subsurface architecture: a moderately conductive near-surface vadose zone (20 to 30 Ohm.m) overlying a thick, highly resistive, and largely dry sedimentary body extending to the maximum investigation depth of 18 m. This deep resistive structure confirms the absence of a shallow saline groundwater body at this site and is consistent with the lower surface salinity detected by the satellite classification. The coherence between the ERT subsurface structure and the K-Means surface classification at both sites validates the reliability of the satellite-based salinity zonation and demonstrates that the two methods are genuinely complementary: satellite data provide the spatial continuity and temporal depth that field surveys cannot achieve, while ERT provides the critical subsurface structural information needed to understand the hydrogeological mechanisms controlling the surface salinity patterns observed from orbit.

Methodologically, the GEE-based workflow developed in this thesis is fully reproducible using freely available satellite data and open-source cloud computing resources. The modular script architecture allows straightforward adaptation to other geographic regions in Algeria and the wider MENA region by modifying the AOI geometry, study period, and sensor parameters. This transferability, combined with the cost-effectiveness of combining free Sentinel-2 data with targeted ERT field campaigns guided by satellite classification, constitutes a scalable and evidence-based protocol for monitoring soil degradation across comparable dryland oasis environments.

Recommendations for Future Work

Based on the findings and limitations of this study, the following recommendations are made for future research:

- Field soil sampling: Soil cores should be collected at locations collocated with ERT profiles and representative satellite pixels to measure ECe, pH, and ion chemistry. This would enable quantitative calibration of remote sensing indices against measured salinity and the establishment of site-specific resistivity-ECe relationships for the Ouargla basin, significantly improving the interpretive rigour of both remote sensing and ERT results.

- Supervised machine learning: Once field-validated ECe data are available, supervised Random Forest or Support Vector Regression classifiers should be trained on GEEextracted spectral index values and compared against the unsupervised K-Means approach in terms of classification accuracy, spatial pattern, and transferability to unsampled areas.
- Extended ERT campaign: Additional ERT profiles across all five K-Means salinity classes and within the zones of highest NDSI temporal variability would provide a comprehensive subsurface characterisation of the full salinity gradient. The combination of ERT with time-domain electromagnetic (TEM) soundings would further improve depth estimation beyond the current ERT depth of investigation and help resolve the deep saline aquifer structure at greater depth.
- Sentinel-1 SAR integration: The combination of Sentinel-1 C-band backscatter, which is sensitive to soil dielectric properties and surface roughness, with the Sentinel-2 optical indices has been shown to improve ECe prediction by 10 to 30 percent in comparable arid environments (Mohamed et al., 2023; Ma et al., 2021) and should be systematically evaluated for the Ouargla study area.
- Hyperspectral data: The PRISMA and EnMAP hyperspectral satellites provide diagnostic absorption features for individual salt minerals (halite, gypsum, mirabilite) that Sentinel-2 multispectral data cannot resolve. Evaluation of these sensors for the Ouargla study area would assess the added value of mineral-level salinity characterisation relative to the multi-index Sentinel-2 approach adopted in this thesis.
- Long-term monitoring: Annual repetition of the GEE multi-index analysis would track the trajectory of salinity change in the study area and allow evaluation of the effectiveness of any drainage or irrigation management interventions implemented in response to the salinity map. Multidecadal analysis using the full Landsat archive (1984 to present) would additionally reveal the historical dynamics of oasis salinisation and the contribution of changing irrigation practices to observed trends.
- Integration with drainage modelling: Combining the salinity zone map with digital elevation models and hydraulic drainage network models would identify the specific agricultural parcels and irrigation canals where drainage improvements would most effectively reduce secondary salinisation, providing the spatial precision required for evidence-based land management planning in the Ouargla oasis system.

In conclusion, this thesis demonstrates that the integration of cost-effective, cloud-computingbased multitemporal Sentinel-2 remote sensing with targeted ERT geophysical field validation constitutes a robust, scalable, and scientifically rigorous protocol for soil salinity assessment in hyperarid oasis environments. The K-Means remote sensing classification and the ERT subsurface characterisation were found to be mutually consistent, with each method revealing a distinct and complementary dimension of the salinisation process: surface spectral expression from satellite and subsurface hydrogeological structure from geophysics. The methodology is directly applicable to the pressing land management challenges of the Ouargla basin and fully transferable to comparable Saharan oasis systems across North Africa and the wider MENA region, where soil salinity continues to threaten the viability of irrigated agriculture under conditions of increasing climatic aridity and groundwater pressure..

References

Abbas, A., Khan, S., Hussain, N., Hanjra, M. A., and Akbar, S. (2013). Characterizing soil salinity in irrigated agriculture using a remote sensing approach. *Physics and Chemistry of the Earth, Parts A/B/C*, 55-57, 43-52. https://doi.org/10.1016/j.pce.2010.12.004

Akca, E., Aydin, M., Kapur, S., Kume, T., Nagano, T., Watanabe, T., and Zorlu, K. (2020). Long-term monitoring of soil salinity in a semi-arid environment of Turkey. *Catena*, 193, 104614. https://doi.org/10.1016/j.catena.2020.104614

Aksoy, S., Yildirim, A., Gorji, T., Hamzehpour, N., Tanik, A., and Sertel, E. (2022). Assessing the performance of machine learning algorithms for soil salinity mapping in Google Earth Engine. *Advances in Space Research*, 69(2), 1072-1086. https://doi.org/10.1016/j.asr.2021.10.024

Allbed, A., Kumar, L., and Aldakheel, Y. Y. (2014). Assessing soil salinity using soil salinity and vegetation indices derived from IKONOS high-spatial resolution imageries: applications in a date palm dominated region. *Geoderma*, 230-231, 1-8. https://doi.org/10.1016/j.geoderma.2014.03.025

Archie, G. E. (1942). The electrical resistivity log as an aid in determining some reservoir characteristics. *Transactions AIME*, 146, 54-62. https://doi.org/10.2118/942054-G

Ayari, S., Gabtni, H., and Zouhri, L. (2023). Imaging seawater flow in porous media under climate change water stress using geophysics: a case study of Menzel Horr coastline in Northeastern Tunisia, Mediterranean basin. *Environmental Earth Sciences*, 82(21), 499. https://doi.org/10.1007/s12665-023-11183-3

Bannari, A., and Al-Ali, Z. M. (2020). Assessing climate change impact on soil salinity dynamics between 1987 and 2017 in arid landscape using Landsat TM, ETM+ and OLI data. *Remote Sensing*, 12(17), 2794. https://doi.org/10.3390/rs12172794

Bouafia, I. E., and Djidel, M. (2013). Evolution du chott et sebkha de la cuvette d'Ouargla par utilisation des images Landsat multi-dates.

Bouderbala, A., Remini, B., and Hamoudi, A. S. (2016). Geoelectrical investigation of saline water intrusion into freshwater aquifers: a case study of Nador coastal aquifer, Tipaza, Algeria. *Geofisica Internacional*, 55(4), 239-253. https://doi.org/10.1016/j.gi.2016.09.001

Douaoui, A. E. K., Nicolas, H., and Walter, C. (2006). Detecting salinity hazards within a semiarid context by means of combining soil and remote-sensing data. *Geoderma*, 134(1-2), 217-230. https://doi.org/10.1016/j.geoderma.2005.10.009

Duan, C., Zhang, Y., Hu, C., Chen, H., and Liu, P. (2025). Soil salinity inversion by combining multi-temporal Sentinel-2 images near the sampling period in coastal salinized farmland. *Frontiers in Environmental Science*, 13, 1533419. https://doi.org/10.3389/fenvs.2025.1533419
El Harti, A., Lhissou, R., Chokmani, K., Ouzemou, J. E., Hassouna, M., Bachaoui, E. M., and

El Ghmari, A. (2016). Spatiotemporal monitoring of soil salinization in irrigated Tadla Plain (Morocco) using satellite spectral indices. *International Journal of Applied Earth Observation and Geoinformation*, 50, 64-73. https://doi.org/10.1016/j.jag.2016.03.008

Escadafal, R. (1989). Remote sensing of arid soil surface color with Landsat Thematic Mapper. *Advances in Space Research*, 9(1), 159-163. https://doi.org/10.1016/02731177(89)90481-X

FAO. (2021). *Global map of salt-affected soils (GSASmap)*. Food and Agriculture Organization of the United Nations, Rome. https://www.fao.org/soils-portal/soil-degradationrestoration/salt-affected-soils/global-map-of-salt-affected-soils/en/

Farifteh, J., Van der Meer, F., Atzberger, C., and Carranza, E. J. M. (2007). Quantitative analysis of salt-affected soil reflectance spectra: a comparison of two adaptive methods (PLSR and ANN). *Remote Sensing of Environment*, 110(1), 59-78. https://doi.org/10.1016/j.rse.2007.02.008

Fethi, M., Faouzi, Z., Mohamed, D., Sofiane, L., and Mei-Ling, H. C. (2023). Effect of a hyperarid climate on groundwater salinity: a case study of the Ouargla shallow aquifer (Northern Sahara, Algeria). *Archives of Environmental Protection*, 49(4). https://doi.org/10.24425/aep.2023.147573

Gao, B. C. (1996). NDWI: a normalized difference water index for remote sensing of vegetation liquid water from space. *Remote Sensing of Environment*, 58(3), 257-266. https://doi.org/10.1016/S0034-4257(96)00067-3

Gitelson, A. A., Gritz, Y., and Merzlyak, M. N. (2003). Relationships between leaf chlorophyll content and spectral reflectance and algorithms for non-destructive chlorophyll assessment in higher plant leaves. *Journal of Plant Physiology*, 160(3), 271-282. https://doi.org/10.1078/0176-1617-00887

Gorji, T., Yildirim, A., Hamzehpour, N., Tanik, A., and Sertel, E. (2020). Soil salinity analysis of Urmia Lake Basin using Landsat-8 OLI and Sentinel-2A based spectral indices and electrical conductivity measurements. *Ecological Indicators*, 112, 106173. https://doi.org/10.1016/j.ecolind.2020.106173

Gorelick, N., Hancher, M., Dixon, M., Ilyushchenko, S., Thau, D., and Moore, R. (2017). Google Earth Engine: planetary-scale geospatial analysis for everyone. *Remote Sensing of Environment*, 202, 18-27. https://doi.org/10.1016/j.rse.2017.06.031

Hadj Kouider, M., Nezli, I., and Hamdi-Aissa, B. (2019). Reconstitution of the surface geology of Ouargla basin-Southern Algeria by remote sensing. *Journal of Al-Hussein University for Research*, 54-64.

Hamdi-Aissa, B., Valles, V., Aventurier, A., and Ribolzi, O. (2004). Soils and brine geochemistry and mineralogy of hyperarid desert playa, Ouargla Basin, Algerian Sahara. *Arid Land Research and Management*, 18(2), 103-126. https://doi.org/10.1080/15324980490280656

Hassani, A., Azapagic, A., and Shokri, N. (2021). Global predictions of primary soil salinization under changing climate in the 21st century. *Nature Communications*, 12(1), 6663. https://doi.org/10.1038/s41467-021-26907-3

Huete, A. R. (1988). A soil-adjusted vegetation index (SAVI). *Remote Sensing of Environment*, 25(3), 295-309. https://doi.org/10.1016/0034-4257(88)90106-X

Huete, A., Didan, K., Miura, T., Rodriguez, E. P., Gao, X., and Ferreira, L. G. (2002). Overview of the radiometric and biophysical performance of the MODIS vegetation indices. *Remote Sensing of Environment*, 83(1-2), 195-213. https://doi.org/10.1016/S00344257(02)00096-2

Idder, T., Idder, A., Cheloufi, H., Benzida, A., Khemis, R., and Moguedet, G. (2013). La surexploitation des ressources hydriques au Sahara algerien et ses consequences sur l'environnement: un cas typique, l'oasis de Ouargla (Sahara septentrional). *Techniques Sciences Methodes*, 5, 31-39.

Jafari, A., Khademi, H., Finke, P. A., Van de Wauw, J., and Ayoubi, S. (2014). Spatial prediction of soil great groups by boosted regression trees using a limited point dataset in an arid region, southeastern Iran. *Geoderma*, 232, 148-163. https://doi.org/10.1016/j.geoderma.2014.04.029

Khan, N. M., Rastoskuev, V. V., Sato, Y., and Shiozawa, S. (2005). Assessment of hydrosaline land degradation by using a simple approach of remote sensing indicators. *Agricultural Water Management*, 77(1-3), 96-109. https://doi.org/10.1016/j.agwat.2004.09.028

Loke, M. H., and Barker, R. D. (1996). Rapid least-squares inversion of apparent resistivity pseudosections by a quasi-Newton method. *Geophysical Prospecting*, 44(1), 131-152. https://doi.org/10.1111/j.1365-2478.1996.tb00142.x

Loke, M. H., Chambers, J. E., Rucker, D. F., Kuras, O., and Wilkinson, P. B. (2013). Recent developments in the direct-current geoelectrical imaging method. *Journal of Applied Geophysics*, 95, 135-156. https://doi.org/10.1016/j.jappgeo.2013.02.017

Luo, Z., Deng, M., Tang, M., et al. (2025). Estimating soil profile salinity under vegetation cover based on UAV multi-source remote sensing. *Scientific Reports*, 15, 2713. https://doi.org/10.1038/s41598-024-82868-9

Ma, G., Ding, J., Han, L., Zhang, Z., and Ran, S. (2021). Digital mapping of soil salinization based on Sentinel-1 and Sentinel-2 data combined with machine learning algorithms. *Regional Sustainability*, 2(2), 177-188. https://doi.org/10.1016/j.regsus.2021.06.001

Mansouri, Z., Leghrieb, Y., Kouadri, S., Al-Ansari, N., Najm, H. M., Mashaan, N. S., and Khedher, K. M. (2022). Hydro-geochemistry and groundwater quality assessment of Ouargla Basin, South of Algeria. *Water*, 14(15), 2441. https://doi.org/10.3390/w14152441

Metternicht, G. I., and Zinck, J. A. (2003). Remote sensing of soil salinity: potentials and constraints. *Remote Sensing of Environment*, 85(1), 1-20. https://doi.org/10.1016/S00344257(02)00188-8

Mohamed, S. A., Metwaly, M. M., Metwalli, M. R., AbdelRahman, M. A. E., and Badreldin, N. (2023). Integrating active and passive remote sensing data for mapping soil salinity using machine learning and feature selection approaches in arid regions. *Remote Sensing*, 15(7), 1751. https://doi.org/10.3390/rs15071751

Naimi, S., Ayoubi, S., Zeraatpisheh, M., and Dematte, J. A. M. (2021). Ground observations and environmental covariates integration for mapping of soil salinity: a machine learningbased approach. *Remote Sensing*, 13(23), 4825. https://doi.org/10.3390/rs13234825

Oldenburg, D. W., and Li, Y. (1999). Estimating depth of investigation in DC resistivity and IP surveys. *Geophysics*, 64(2), 403-416. https://doi.org/10.1190/1.1444545

Paz, M. C., Castanheira, N. L., Paz, A. M., Goncalves, M. C., Monteiro Santos, F., and Farzamian, M. (2024). Comparison of electromagnetic induction and electrical resistivity tomography in assessing soil salinity: insights from four plots with distinct soil salinity levels. *Land*, 13(3), 295. https://doi.org/10.3390/land13030295

Rengasamy, P. (2006). World salinization with emphasis on Australia. *Journal of Experimental Botany*, 57(5), 1017-1023. https://doi.org/10.1093/jxb/erj108

Richards, L. A. (Ed.). (1954). *Diagnosis and improvement of saline and alkali soils* (USDA Agricultural Handbook No. 60). US Government Printing Office. https://www.ars.usda.gov/ARSUserFiles/20360500/hb60_pdf/hb60complete.pdf

Rikimaru, A., Roy, P. S., and Miyatake, S. (2002). Tropical forest cover density mapping. *Tropical Ecology*, 43(1), 39-47.

Rouse, W. (1973). Monitoring vegetation system in the great plain with ERTS. In *3rd ERTS symposium, NASA Washington DC, 1973* (Vol. 1, pp. 309-317).

Roy, D. P., and Yan, L. (2020). Robust Landsat-based crop time series modelling. *Remote Sensing of Environment*, 238, 110810. https://doi.org/10.1016/j.rse.2018.11.038

Sabrine, S., Drias, A., Nemer, Z., and Taibi, Y. (2025). Degradation assessment of the M'Zab Valley oases in Algeria. *Papers in Applied Geography*, 11(1), 94-118. https://doi.org/10.1080/23754931.2024.2360482

Samouëlian, A., Cousin, I., Tabbagh, A., Bruand, A., and Richard, G. (2005). Electrical resistivity survey in soil science: a review. *Soil and Tillage Research*, 83(2), 173-193. https://doi.org/10.1016/j.still.2004.10.004

Shahid, S. A., Abdelfattah, M. A., Omar, S. A., Harahsheh, H., Othman, Y., and Mahmoudi, H. (2010). Mapping and monitoring of soil salinization using remote sensing, GIS, modelling, electromagnetic induction and conventional methods: case studies. In *Proceedings of the International Conference on Soils and Groundwater Salinization in Arid Countries* (Vol. 59, p. 97).

Singh, A. (2021). Soil salinization management for sustainable development: a review. *Journal of Environmental Management*, 277, 111383. https://doi.org/10.1016/j.jenvman.2020.111383

Sirpa-Poma, J. W., Satge, F., Resongles, E., et al. (2023). Towards the improvement of soil salinity mapping in a data-scarce context using Sentinel-2 images in machine-learning models. *Sensors*, 23(23), 9328. https://doi.org/10.3390/s23239328

Taghizadeh-Mehrjardi, R., Minasny, B., Sarmadian, F., and Malone, B. P. (2014). Digital mapping of soil salinity in Ardakan region, central Iran. *Geoderma*, 213, 15-28. https://doi.org/10.1016/j.geoderma.2013.07.020

Taghizadeh-Mehrjardi, R., Schmidt, K., Toomanian, N., Heung, B., Behrens, T., Mosavi, A., and Scholten, T. (2021). Improving the spatial prediction of soil salinity in arid regions using wavelet transformation and support vector regression models. *Geoderma*, 383, 114793. https://doi.org/10.1016/j.geoderma.2020.114793

Wang, J., Ding, J., Yu, D., Teng, D., He, B., Chen, X., Ge, X., Zhang, Z., Wang, Y., Yang, X., Shi, T., and Su, F. (2020). Machine learning-based detection of soil salinity in an arid desert region, Northwest China: a comparison between Landsat-8 OLI and Sentinel-2 MSI. *Science of the Total Environment*, 707, 136092. https://doi.org/10.1016/j.scitotenv.2019.136092

Wang, J., Ding, J., Wang, L., and Yang, M. (2021). Soil salinity mapping using machine learning algorithms with Sentinel-2 MSI in arid areas, China. *Remote Sensing*, 13(2), 305. https://doi.org/10.3390/rs13020305

Wen, Y. (2025). A new vegetation structural scattering index (VSSI) using a kernel-driven BRDF model based on Fengyun-4A/ARGI data. *Remote Sensing Applications: Society and Environment*, 37, 101501. https://doi.org/10.1016/j.rsase.2024.101501

Yahiaoui, I., Douaoui, A., Zhang, Q., and Ziane, A. (2015). Soil salinity prediction in the Lower Cheliff plain (Algeria) based on remote sensing and topographic feature analysis. *Journal of Arid Land*, 7(6), 794-805. https://doi.org/10.1007/s40333-015-0053-9

You, Y., Fu, W., Liu, H., Li, G., Wang, S., Pan, X., and Wang, C. (2025). Assessing fieldscale salt leaching during saline soil remediation with electrical resistivity tomography and electromagnetic induction methods. *Frontiers in Environmental Science*, 13, 1745613. https://doi.org/10.3389/fenvs.2025.1745613

Zhang, J., Ding, J., Wang, J., Zhang, Z., Tan, J., and Ge, X. (2024). Spatial heterogeneity response of soil salinization inversion based on deep learning. *Frontiers in Plant Science*, 15, 1437390. https://doi.org/10.3389/fpls.2024.1437390

Zhang, J., Ge, X., Hou, X., Han, L., Zhang, Z., Feng, W., and Luo, X. (2025). Strategies for soil salinity mapping using remote sensing and machine learning in the Yellow River Delta. *Remote Sensing*, 17(15), 2619. https://doi.org/10.3390/rs17152619